Spins, Moments and Radii of Cd Isotopes

Dissertation

zur Erlangung des Grades
”Doktor der Naturwissenschaften”

im Promotionsfach Chemie
am Fachbereich Chemie, Pharmazie und Geowissenschaften
der Johannes Gutenberg-Universität
in Mainz

CERN-THESIS-2013-354
28/11/2013

Michael Hammen
geb. in Mainz

Mainz, den 30.10.2013

Abstract

The complex nature of the nucleon-nucleon interaction and the wide range of systems covered by the roughly 3000 known nuclides leads to a multitude of effects observed in nuclear structure. Among the most prominent ones is the occurence of shell closures at so-called "magic numbers", which are explained by the nuclear shell model. Although the shell model already is on duty for several decades, it is still constantly extended and improved. For this process of extension, fine adjustment and verification, it is important to have experimental data of nuclear properties, especially at crucial points like in the vicinity of shell closures. This is the motivation for the work performed in this thesis: the measurement and analysis of nuclear ground state properties of the isotopic chain of $^{100-130}$Cd by collinear laser spectroscopy .

The experiment was conducted at ISOLDE/CERN using the collinear laser spectroscopy apparatus COLLAPS. This experiment is the continuation of a run on neutral atomic cadmium from $A = 106$ to $A = 126$ and extends the measured isotopes to even more exotic species. The required gain in sensitivity is mainly achieved by using a radiofrequency cooler and buncher for background reduction and by using the strong $5s\ ^2\mathrm{S}_{1/2} \rightarrow 5p\ ^2\mathrm{P}_{3/2}$ transition in singly ionized Cd. The latter requires a continuous wave laser system with a wavelength of 214.6 nm, which has been developed during this thesis. Fourth harmonic generation of an infrared titanium sapphire laser is achieved by two subsequent cavity-enhanced second harmonic generations, leading to the production of deep-UV laser light up to about 100 mW.

The acquired data of the $Z = 48$ Cd isotopes, having one proton pair less than the $Z = 50$ shell closure at tin, covers the isotopes from $N = 52$ up to $N = 82$ and therefore almost the complete region between the neutron shell closures $N = 50$ and $N = 82$. The isotope shifts and the hyperfine structures of these isotopes have been recorded and the magnetic dipole moments, the electric quadrupole moments, spins and changes in mean square charge radii are extracted. The obtained data reveal among other features an extremely linear behaviour of the quadrupole moments of the $I = 11/2^-$ isomeric states and a parabolic development in differences in mean square nuclear charge radii between ground and isomeric state. The development of charge radii between the shell closures is smooth, exposes a regular odd-even staggering and can be described and interpreted in the model of Zamick and Thalmi.

Zusammenfassung

Die komplexe Natur der Nukleon-Nukleon Wechselwirkung und die große Bandbreite zusammengesetzter Systeme, die sich in den etwa 3000 bekannten Nukliden wiederspiegelt, führen zu einer Vielzahl beobachteter Kernstruktureffekte. Einer der markantesten unter ihnen ist das Auftauchen von Schalenabschlüssen bei den sogenannten "magischen Zahlen", welche durch das Kernschalenmodell erklärt werden können. Obwohl dieses Modell bereits seit mehreren Jahrzehnten in Verwendug ist, wird es immer noch fortlaufend erweitert und verbessert. Elementare Grundlage für diesen Prozess der Erweiterung, Feinjustage und Verifikation ist der Vergleich mit experimentellen Daten zu Kernstrukturgrößen. Dies gilt insbesondere für kritische und zentrale Stellen, wie sie beispielsweise die Umgebungen der magischen Zahlen darstellen. Diese Tatsache ist die Motivation für die im Rahmen dieser Arbeit durchgeführten Messungen: die Vermessung und Analyse von Grundzustandseigenschaften der Isotopenreihe $^{100-130}$Cd mittels kollinearer Laserspektroskopie.

Das Experiment wurde an ISOLDE/CERN mit der Apparatur zur kollinearen Laserspektroskopie COLLAPS durchgeführt. Die Messungen stellen die Fortführung einer Strahlzeit an neutralen Atomen der Cadmiumisotope zwischen $A = 106$ und $A = 126$ dar und erweitern die damals gemessenen Nuklide um noch exotischere Kerne. Die hierfür erforderliche Steigerung der Nachweissensitivität wird im Wesentlichen durch die Verwendung eines Radiofrequenz Cooler and Bunchers zur Unterdrückung des Untergrundrauschens und die Spektroskopie des starken $5s\ ^2\mathrm{S}_{1/2} \to 5p\ ^2\mathrm{P}_{3/2}$ Übergangs im einfach ionisierten Cadmium erreicht. Letzteres erfordert ein Dauerstrich-Lasersystem mit einer Wellenlänge von 214.6 nm, welches im Rahmen dieser Arbeit entwickelt wurde. Hierbei wird die vierte Harmonische eines Titan-Saphir-Lasers durch zwei aufeinanderfolgende Verdopplungen in Überhöhungsresonatoren erreicht, wodurch bis zu 100 mW Laserlicht im tiefen UV produziert werden können.

Die gewonnenen Daten von $Z = 48$ Cd-Isotopen, welche ein Protonenpaar weniger als der Kernschalenabschluss bei $Z = 50$ besitzen, erstrecken sich von $N = 52$ bis hin zu $N = 82$. Damit decken sie fast die gesamte Region zwischen den beiden Schalenabschlüssen $N = 50$ und $N = 82$ ab. Die Isotopieverschiebungen und dir Hyperfeinstrukturen dieser Isotope wurden gemessen und daraus die magnetischen Dipolmomente, die elektrischen Quadurpolmomente, Spins und Änderungen der mittleren quadratischen Kernladungsradien extrahiert. Diese Daten zeigen unter anderem ein extrem lineares Verhalten der Quadrupolmomente im isomeren Zustand mit Spin $I^\pi = 11/2^-$ sowie einen parabolischen Verlauf in der Differenz der mittleren quadratischen Ladungsradien zwischen Grundzustand und Isomer. Der Verlauf der Ladungsradien zwischen den beiden Schalenabschlüssen ist kontinuierlich, weist ein reguläres odd-even staggering auf und kann sehr gut im Rahmen des Modells von Zamick und Thalmi beschrieben und interpretiert werden.

Contents

1. Introduction and Motivation 1

2. Theory 3

2.1. Atomic Theory . . . 3
  2.1.1. Selection Rules and Line Shapes . . . 3
  2.1.2. Isotope Shift . . . 4
  2.1.3. Hyperfine Splitting . . . 6
  2.1.4. Spectra . . . 8
2.2. Collinear Laser Spectroscopy . . . 10
2.3. Nuclear Models and Properties . . . 11
  2.3.1. Liquid Drop and Droplet Model . . . 11
  2.3.2. Nuclear Shell Model . . . 11
  2.3.3. Magnetic Moments . . . 12
  2.3.4. Electric Quadrupole Moments . . . 15
  2.3.5. Nuclear Charge Radii . . . 16

3. Experiment 19

3.1. Setup . . . 19
  3.1.1. The Cd-Experiment . . . 19
  3.1.2. ISOLDE . . . 19
  3.1.3. COLLAPS Beamline . . . 22
  3.1.4. Laser System . . . 23
  3.1.5. Data Acquisition . . . 28

4. Analysis and Interpretation 31

4.1. Fitting the Spectra and Spin Determination . . . 31
  4.1.1. Calculating the Rest Frame Frequency . . . 31
  4.1.2. Uncertainty Estimation of the Number of Counts . . . 32
  4.1.3. Lineshape Determination . . . 33
  4.1.4. A-ratio and Hyperfine Anomaly . . . 34
  4.1.5. Spin Determination and Identification . . . 35
  4.1.6. ^{129}Cd . . . 36

4.2. Moments . . . 36
  4.2.1. Magnetic Moment . . . 39
  4.2.2. Quadrupole Moment . . . 41
4.3. Radii . . . 44
  4.3.1. King-plot . . . 45

5. Summary and Outlook **55**

A. Appendix **57**
A.1. Masses . . . 57
A.2. Comparison of Nuclear Moments . . . 57
A.3. Comparison of Radii . . . 57

List of Figures

2.1. The Field Shift 5

2.2. Mass and field shift depending on Z 6

2.3. Hyperfine Levels of cadmium 8

2.4. Theortically calculated hyperfine spectra 9

2.5. Single Particle Levels in the Nuclear Shell Modell 13

3.1. ISOLDE layout 20

3.2. Radiofrequency cooler and buncher 21

3.3. Time of flight spectra 22

3.4. The COLLAPS beamline 23

3.5. Cd level scheme 23

3.6. Laser setup sketch 26

3.7. Laser setup 27

3.8. Higher harmonic generation efficiency 27

3.9. Data Acquisition 28

4.1. RFQ voltage 32

4.2. Spectra of ^{114}Cd 33

4.3. Influence of A-ratio fixing 34

4.4. Cd Energy Levels 35

4.5. Spectra of odd isotopes for $A = 119 - 129$ 37

4.6. Spectra of ^{125,129}Cd 38

4.7. Magnetic moments 41

4.8. Magnetic moments 43

4.9. Quadrupole moments of the 11/2 state of Cd and Sn 44

4.10. King-plot 46

4.11. Differences in mean square charge radii of cadmium 48

4.12. Modified isotope shift 49

4.13. Differences of mean square charge radii in the mass region of tin 51

4.14. Difference in ms charge radius between ground and isomeric state 52

4.15. Comparison of differences in ms charge radius to theoretical calculations . . . 52

A.1. Magnetic moment comparison of the ground state 59

A.2. Magnetic moment comparison of the isomeric state 59
A.3. Quadrupole moment comparison of the ground state 60
A.4. Quadrupole moment comparison of the isomeric state 60
A.5. Comparison of charge radii 61
A.6. RFQ voltage and reference line center 62

List of Tables

2.1. Schmidt moments 14

4.1. A-factors and magnetic moments 40
4.2. B-Factors and quadrupole moments 42
4.3. Mean square charge radii 50

A.1. Isotope masses 58

1. Introduction and Motivation

The nuclear shell model is one of the most successful descriptions of atomic nuclei. First proposed by M. Goeppert-Mayer and J. H. D. Jensen [GMJ55], it is capable of explaining the shell closures of protons and neutrons. There, binding energy is increased relative to surrounding nuclei, adding stability and decreasing their size. Consequently, the shell model is most accurate in the vicinity of those closed shells, where the independent particle approximation, upon which the shell model is based, is most applicable. The nuclear shell model has good predictive power for e.g. spin, parity, energy, and magnetic moment of the existing states. Additionally, it is intriguingly simple and intuitive, as many basic calculations can be solved analytically.

Nevertheless, increasing the number of particles outside of closed shells, especially for protons and neutrons simultaneously, leads to residual interactions and thereby to deviations from the nuclear shell model, which can be compensated by introducing perturbational effects, for example core-polarization. In this region, usually assumed to be about up to 2 particles away from the closed shell, the limits of the model can be probed by measurements of experimental observables. The experimental determination of nuclear ground state properties is essential for the development and improvement of nuclear models. New effects and their systematics can be studied and the properties of exotic species are used for fine tuning of the existing model parameters.

Laser spectroscopic determinations of the changes in mean-square nuclear charge radii, magnetic moments and electric quadrupole moments are of high quality since they are extracted in a nuclear-model independent way from the observed spectra. Even though there is usually some uncertainty in the determination of the hyperfine fields, the systematic uncertainty caused by this is in most cases sufficiently small to provide benchmark tests for nuclear structure theory. This thesis describes the measurement of the cadmium isotopic chain with the collinear laser spectroscopy apparatus COLLAPS at ISOLDE/CERN. With 2 protons less than the magic proton nucleus tin, cadmium should be well described by the nuclear shell model, yet it should be already significantly influenced by the missing proton pair. It is therefore an ideal candidate for testing this theory. Additionally, the accessibility of nuclei far from stability at radioactive ion beam facilities in this mass region allows to cover almost the complete neutron shell between the magic numbers $N = 50$ and $N = 82$.

2. Theory

2.1. Atomic Theory

Investigation of the distinct structure of the electronic energy levels of atoms and molecules reveals important insights into these systems. Usually this is done in the form of spectroscopy, where transitions between levels are probed and thereby their differences in energy are measured. This started with the discovery of the spectral lines themselves by Fraunhofer and, with increasing resolution, subsequently revealed the fine and hyperfine structure. While the initial energy levels and the fine structure can be explained with electrons in a coulomb field, i.e. a point like electric charge in the center, the hyperfine structure is caused by the nuclear structure and the coupling of the electrons to it. Thereby spectroscopy with sufficiently high precision, which is provided today by laser spectroscopy, allows extraction of nuclear properties from the atomic spectra. The basic theory is discussed in this section.

2.1.1. Selection Rules and Line Shapes

As the energy levels can not be measured directly, spectroscopy investigates transitions between them and thereby energy differences between an initial (i) and a final (f) state. The electric dipole transition (E1) is the strongest and most common type. Its strength is proportional to the matrix element of the dipole operator $\boldsymbol{d} = e < \boldsymbol{r} >$ [Dem05]. It connects levels of unlike parity $\pi_f = -\pi_i$, $\delta L = \pm 1$ [1] and $\delta J = 0,\ \pm 1$ except $J = 0 \rightarrow J = 0$, as can be deduced from conservation of angular momentum and the intrinsic spin of the photon being 1.

The deexciting atom can be described as a fast oscillating electromagnetic dipole with exponentially decreasing amplitude

$$A(t) = \sin(\omega t) \cdot \mathrm{e}^{-t/\tau} \tag{2.1}$$

---

[1] In this thesis δ is used for differences, while Δ marks uncertainties

with the transition frequency $\nu = \omega/(2\pi)$ and the lifetime of the upper level τ. For simplicity the lower level is assumed to be the ground state. The fourier transformation of the time spectrum results in a lorenzian in the frequency space

$$S(\nu) = \frac{1}{\pi} \frac{\gamma/2}{\gamma^2/4 + (\nu - \nu_0)^2} \ . \tag{2.2}$$

The natural linewidth γ is determined by the transition strength $A_{ki} = 1/\tau$: $\gamma = A_{ki}/2\pi$. Additional lifetime decreasing or phase disturbing processes lead to a broadening of this linewidth, but do not alter the shape.

Another common effect is the Doppler broadening. The gaussian velocity distribution, as present in the case of thermal equilibrium, influences the line shape through the Doppler effect. This leads to a voigt profile, which is a convolution of a lorenzian and a gaussian

$$S(\nu) = \int G(\tau) L(\nu - \tau) d\tau = \int \frac{\mathrm{e}^{\frac{-\tau^2}{2\sigma^2}}}{\sigma\sqrt{2\pi}} \cdot \frac{\gamma/2}{\pi((\nu - \tau)^2 + (\gamma/2)^2)} \, d\tau \ . \tag{2.3}$$

In spectroscopy usually the important quantity is the central frequency of the transition. Although it is not necessary to always fully understand the line shape, for accurate results it is at least necessary to have a good mathematical description. Here, the voigt profile is a good choice as it is very flexible and covers a lot of possible influences on the line shape.

2.1.2. Isotope Shift

Due to the electron-electron interaction it is usually impossible to calculate absolute transition frequencies in multi-electron systems with sufficient precision to directly extract the influence of the nucleus on the central line position. However, if the line positions of different isotopes of an element are compared a frequency shift is observed. This is the so called isotope shift $\delta\nu_{\mathrm{IS}}^{A,A'} = \nu^A - \nu^{A'}$. It is the sum of the mass shift $\delta\nu_{\mathrm{MS}}^{A,A'}$ and the field shift $\delta\nu_{\mathrm{FS}}^{A,A'}$ and can therfore be written as

$$\delta\nu_{\mathrm{IS}}^{A,A'} = \delta\nu_{\mathrm{MS}}^{A,A'} + \delta\nu_{\mathrm{FS}}^{A,A'} \ . \tag{2.4}$$

The mass shift is caused by the recoil motion of the nucleus, which influences the reduced mass of the electron in the center of mass system (barycenter). In a simple one-electron system, this effect is proportional to

$$\delta\nu_{\mathrm{NMS}}^{A,A'} = K_{\mathrm{NMS}} \cdot \frac{m^A - m^{A'}}{m^A m^{A'}} \tag{2.5}$$

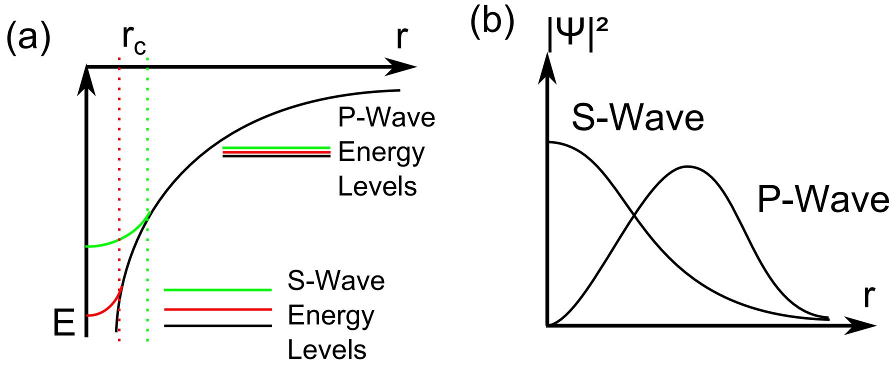

Figure 2.1.: (a) Sketch of the deviation from the coulomb potential for different charge radii and principal influence on the energy levels. (b) S-waves have a larger probability to be inside the nucleus than higher angular momentum states and therefore are influenced stronger by the finite size effect.

with the nuclear masses m^A and the normal mass shift constant $K_{\mathrm{NMS}} = m_e\nu$. This is altered by the correlation between the electrons and the corresponding shift can be expressed by

$$\delta\nu_{\mathrm{SMS}}^{A,A'} = K_{\mathrm{SMS}} \cdot \frac{m^A - m^{A'}}{m^A m^{A'}} \ . \tag{2.6}$$

To calculate the specific mass shift constant K_{SMS}, the electronic wave functions have to be determined to a high degree, which usually leads to insufficient accuracy for the extraction of nuclear properties. As it has the same mass dependence as the normal mass shift, both can be combined to the total mass shift:

$$\delta\nu_{\mathrm{MS}}^{A,A'} = (K_{\mathrm{NMS}} + K_{\mathrm{SMS}}) \cdot \frac{m^A - m^{A'}}{m^A m^{A'}} = K \cdot M \ . \tag{2.7}$$

The field shift on the other hand is caused by the deviation of the electric field from the coulomb potential inside the nucleus as shown in Fig. 2.1. It is proportional to the differences of the mean square nuclear charge radii and the change of the probability density of the electron inside the nucleus:

$$\delta\nu_{\mathrm{FS}}^{A,A'} = \frac{Ze^2}{6h\epsilon_0}\Delta|\Psi(0)|^2\delta\langle r^2\rangle^{A,A'} = F \cdot \delta\langle r^2\rangle^{A,A'} \ . \tag{2.8}$$

Here, the probability density $|\Psi(x)|^2$ is assumed to be constant within the nuclear volume, which is a good approximation for light and medium heavy nuclei. Hence it usually influences the energy of S-levels strongest and $S \to P$ transitions are most sensitive to changes in ms charge radii, as there the difference $\Delta|\Psi(0)|^2 = |\Psi_f(0)|^2 - |\Psi_i(0)|^2$ is rather large.

Taking these effects into account, the isotope shift can be expressed by

$$\delta\nu_{\mathrm{IS}}^{A,A'} = K \cdot M + F \cdot \delta\langle r^2\rangle^{A,A'}. \tag{2.9}$$

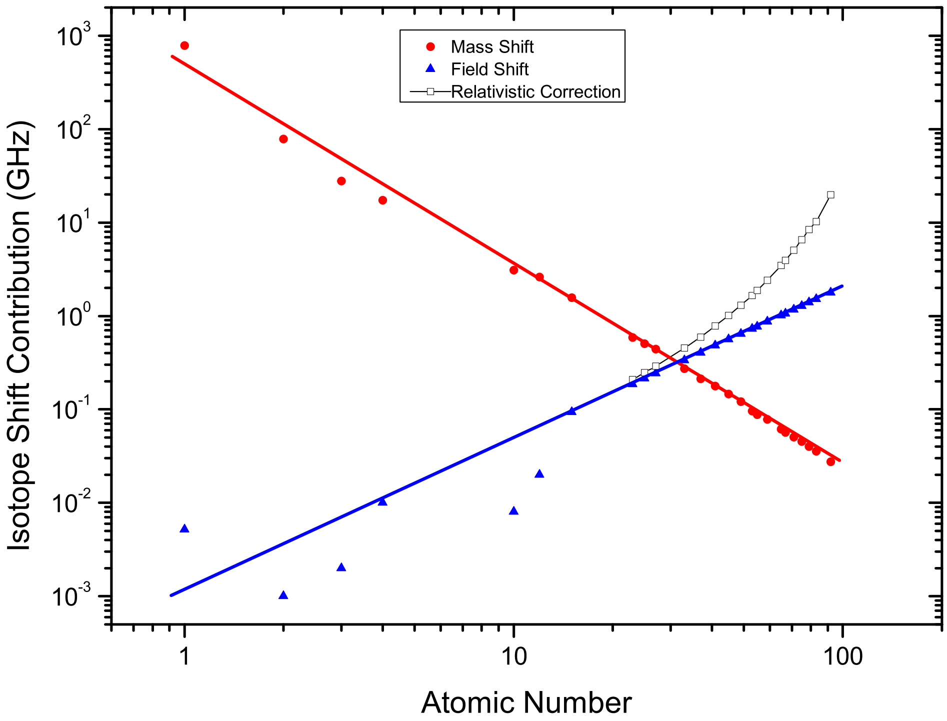

Figure 2.2.: Development of mass and field shift with atomic number Z. Plotted points are experimental values for elements up to $Z = 11$ (Na). For higher Z they are extrapolated. [Bla13] While for light masses the mass shift is dominating the isotope shift, around $Z = 30$ the field shift becomes the larger contribution.

For light isotopes the relative mass difference between isotopes is large, so the mass shift is the dominating contribution to the isotope shift. For heavy nuclei, $|\Psi(0)|^2$ becomes larger, while relative mass differences get smaller, so the field shift becomes dominant. The approximate scaling of this behaviour is shown in Fig. 2.2. Thus, higher accuracy is required in isotope shift measurements for light elements while for heavier elements it is not as demanding to extract changes in mean square charge radii.

The mass and field shift factor can be determined by the Kingplot procedure. This is explained in detail in Sec. 4.3, where it is conducted for the Cd isotopes.

2.1.3. Hyperfine Splitting

An obvious effect of the hyperfine structure is the splitting of the fine structure lines caused by the magnetic dipole interaction of the nuclear magnetic moment

$$\boldsymbol{\mu_I} = g_I \mu_N \frac{\boldsymbol{I}}{\hbar} \tag{2.10}$$

with the magnetic field created by the electrons at the position of the nucleus

$$\boldsymbol{B}_\mathrm{e} = B_0 \frac{\boldsymbol{J}}{\hbar} \ . \tag{2.11}$$

Here, $\mu_N = e\hbar/2m_p$ is the nuclear magneton, m_p the proton mass, $\boldsymbol{I}$ the nuclear spin and $\boldsymbol{J} = \boldsymbol{L} + \boldsymbol{S}$ the total angular momentum of the electron from the coupling of the orbital momentum $\boldsymbol{L}$ and the spin $\boldsymbol{S}$. This interaction shifts the level energies by[SH08]

$$H_\mathrm{MD} = \boldsymbol{\mu_I} \cdot \boldsymbol{B}_\mathrm{e} = g_I \mu_N B_0 \frac{(\boldsymbol{I} \cdot \boldsymbol{J})}{\hbar^2} \ . \tag{2.12}$$

The last term couples the vectors $\boldsymbol{I}$ and $\boldsymbol{J}$ to the new total angular momentum $\boldsymbol{F} = \boldsymbol{I} + \boldsymbol{J}$. Allowed quantum numbers are

$$|I - J| \leq F \leq |J + I| \tag{2.13}$$

and their eigenstates $|F, m_F\rangle$ characterized by F and it's projection onto the quantization axis m_F fulfill the relations

$$\boldsymbol{F}^2 |F m_F\rangle = \hbar^2 F(F+1) |F m_F\rangle \tag{2.14}$$

$$\boldsymbol{F}_\mathrm{z} = m_F \hbar |F m_F\rangle \ . \tag{2.15}$$

The vector product can then be rewritten as

$$\boldsymbol{I} \cdot \boldsymbol{J} = \frac{1}{2} \left(\boldsymbol{F}^2 - \boldsymbol{I}^2 - \boldsymbol{J}^2 \right) \ . \tag{2.16}$$

This leads to the energy shift of the magnetic dipole interaction

$$H_\mathrm{MD} = \frac{A}{2} \left(F(F+1) - I(I+1) - J(J+1) \right) = \frac{A}{2} K \ , \tag{2.17}$$

with the magnetic-dipole coupling constant $A = g_I \mu_N B_0$.

In this simple picture, the different electronic levels have a constant A-factor ratio which is determined by $B_0(0)$ and J. This is only exact for a point-like magnetic dipole. In the nucleus, the magnetic dipole moment is distributed over the whole nucleus, which has an impact on the hyperfine structure. This effect is called Bohr-Weisskopf-Effect and, as it can effect different fine structure levels in a different way, leads to a change in the A-factor ratio between different isotopes, which is called hyperfine anomaly. It is usually below 1% and can, in most cases, not be resolved by laser spectroscopy. Instead, it is usually investigated using NMR.

Another contribution which shifts the hyperfine levels against each other originates from a non-spherical charge distribution $\rho(\boldsymbol{r})$ inside the nucleus. This leads to a spectroscopic

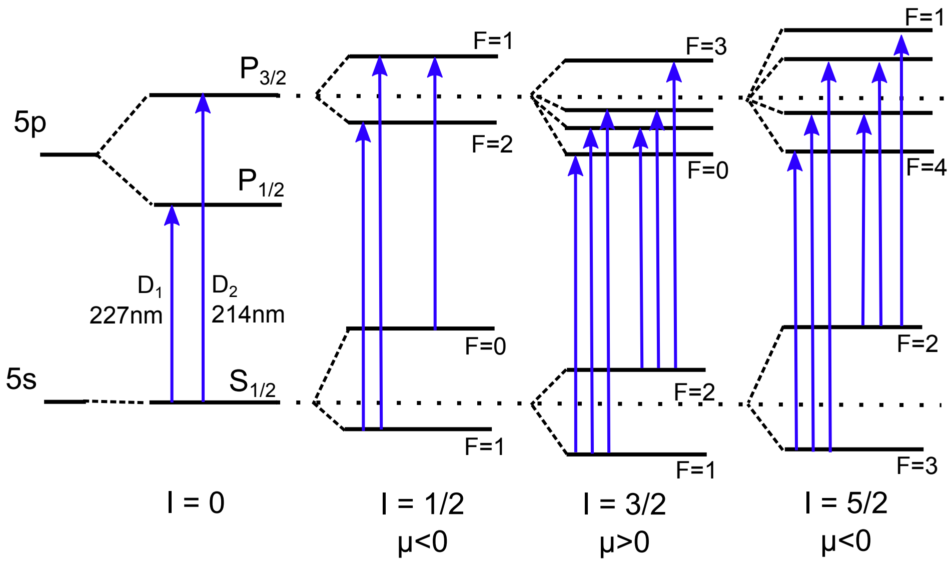

Figure 2.3.: The relevant hyperfine levels of the cadmium ion and allowed transitions between them for different nuclear spins and their expected magnetic moment. Energy levels are not to scale.

quadrupole moment Q_s and interacts with the electric quadrupole field caused by the electrons at the position of the nucleus

$$\langle V_{zz} \rangle = \left. \frac{\partial^2 V}{\partial z^2} \right|_{r=0} . \tag{2.18}$$

The result is a shift in energy levels of

$$H_{EQ} = B \frac{\frac{3}{4} K(K+1) - I(I+1)J(J+1)}{2I(2I-1)J(2J-1)} \tag{2.19}$$

with the electric-quadrupole coupling constant $B = eQ_s \langle V_{zz} \rangle$. The detailed calculation can be found for example in [SH08]. One should note that $\langle V_{zz} \rangle = 0$ for $J \leq 1/2$, so there is no quadrupole shift in those levels. Furthermore, there is no quadrupole shift in nuclei with $I \leq 1/2$, as is explained in Sec. 2.3.

2.1.4. Spectra

The hyperfine levels for the lowest lying levels of an alkaline-like system (as Cd^+ is) are shown in Fig. 2.3. The evolution from gross to hyperfine structure is shown for the $S_{1/2}$ and $P_{3/2}$ levels relevant for this work for nuclear spins from 1/2 to 5/2 with the sign of magnetic moment assumed for those nuclei from the shell model. The $P_{1/2}$ level shows the same splitting as $S_{1/2}$. As already discussed in Sec. 2.1.1, spectroscopy accesses transitions and therefore measures energy differences between the levels. The electric dipole allowed E1 transitions are plotted in the figure as arrows. The selection rule in the hyperfine levels is

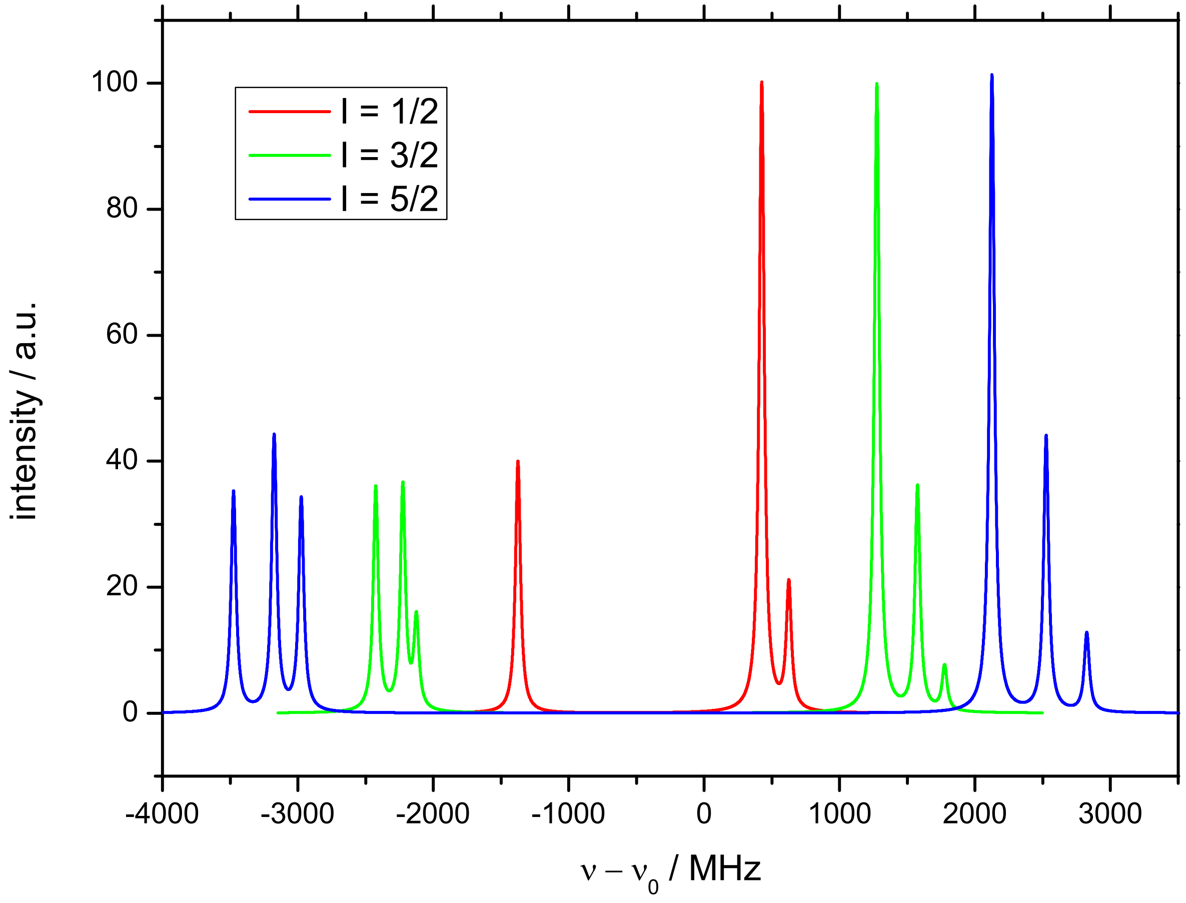

Figure 2.4.: Spectra calculated for nuclei with $I = 1/2$, $I = 3/2$ and $I = 5/2$, $A_\mathrm{l} = -2000\,\mathrm{MHz}$ and $A_\mathrm{u}/A_\mathrm{l} = 0.05$. The number of lines is unique for $I = 1/2$, whereas differences between higher spins are less obvious.

$\Delta F = 0, \ \pm 1$, additionally to the selection rules for fine structure transitions. Each of the resulting lines has the same lineshape as without hyperfine splitting. If one of the energy splittings of upper and lower state is much larger than the other, this leads to multiplets in which several lines are clustered together. The intensities are proportional to the matrix elements of the dipole operator. They can be expressed with the Wigner-6j symbols [Dra06]

$$S_{FF'} = (2F+1)(2F'+1) \begin{Bmatrix} F & F' & 1 \\ J' & J & I \end{Bmatrix} S_{JJ'} \ , \tag{2.20}$$

where $S_{JJ'}$ represents the transition strength of the pure fine structure transition.

With these assumptions one can calculate the expected hyperfine spectra for the different nuclear spins discussed above. The result is plotted in Fig. 2.4. A magnetic hyperfine coupling constant of $A_\mathrm{l} = -2000\,\mathrm{MHz}$ is assumed for the lower level and an A-factor ratio of $A_\mathrm{u}/A_\mathrm{l} = 0.05$. The electric quadrupole interaction is neglected. The model lineshape is a pure lorenzian with a natural linewidth of $\gamma = 45\,\mathrm{MHz}$. One can see that the difference between $I = 1/2$

and $I = 3/2$ is immediately obvious due to the different number of allowed transitions, while for higher spins the number is limited by J and only the relative intensities change slightly.

It is important to note that the relative intensities of a spectrum can be altered to a large degree by optical pumping. The theoretical relative intensities are only accurate in the limit of vanishing laser power, which is of course unfeasible as it reduces sensitivity.

2.2. Collinear Laser Spectroscopy

High resolution spectroscopy can be performed by shining in a laser with a well defined frequency into a sufficiently thin gaseous sample. By tuning the frequency and detecting the response, for example by measuring the photon scattering rate (fluorescence detection), one can determine the transition frequencies. However, accuracy is limited by the Doppler broadening due to the temperature-related movement of the sample, which causes a linewidth of

$$\Delta\nu_{\mathrm{D}} = \frac{\nu_0}{c}\sqrt{\frac{8k_{\mathrm{B}}T\ln 2}{m}}, \tag{2.21}$$

which is typically on the order of several GHz for hot ion sources, 2-3 orders of magnitude larger than a typical natural linewidth of dipole-allowed transitions. Many different techniques have been developed to solve this problem like saturation spectroscopy, Doppler-free two-photon transitions or trapping and cooling [Dem07], either using a spectroscopic technique which is independent of the Doppler effect or by better preparation (cooling) of the sample. For short-lived radioactive isotopes, sample preparation is in most cases impossible or at least complicated due to the often very low preparation efficiency.

In collinear laser spectroscopy the radioactive isotopes, which are transported as ion beam with energies of 30-60 keV, are in flight superimposed with a laser in collinear geometry. Here, one utilizes the fact that during an electrostatic acceleration of the ion beam in the source the energy spread is constant. This leads to a decrease in the width of the velocity distribution

$$\frac{\delta v_U}{\delta v_0} = \frac{\frac{k_{\mathrm{B}}T}{\sqrt{2eUm}}}{\frac{\sqrt{2k_{\mathrm{B}}T}}{m}} = \frac{1}{2}\sqrt{\frac{k_{\mathrm{B}}T}{eU}}, \tag{2.22}$$

which has first been shown by Kaufmann[Kau76]. The resulting Doppler broadening is in the order of typical natural linewidths, allowing high-resolution laser spectroscopy on species with half-lifes down to several ms [Kri12]. A disadvantage is a systematic error of the absolute transition frequency due to the uncertainty of the acceleration voltage. This can be largely compensated, although not for the lightest elements, by measuring frequency differences. This is the case for hyperfine splitting and isotope shift measurements.

In collinear laser spectroscopy usually instead of scanning the laser frequency the ion velocity is changed, leading to a shifted laser frequency in the rest frame of the ion due to the Doppler effect. This is known as Doppler-tuning.

2.3. Nuclear Models and Properties

Since the discovery of the atomic nucleus by Ernest Rutherford in 1911 [Rut11] physics tried to describe its composition and structure. The subsequent discovery of the proton (E. Rutherford, 1920) and the neutron (W. Bothe, H. Becker and J. Chadwick, 1932) [Pea89] answered the question of which particles the nucleus is composed of. Several models were developed to explain the structure of nuclei, yet even today no single model is capable of accurately describing the wide variety of effects observed throughout the nuclear chart. In this section the two models most relevant for this thesis as well as their predictions for nuclear moments and radii are summarized.

2.3.1. Liquid Drop and Droplet Model

One of the most clear and descriptive models is the liquid drop model [BWW01]. This macroscopic model assumes that the nuclear matter forms a liquid drop of constant density with a sharp surface, where neutrons and protons are distributed equally. It leads for example to the semi-empirical mass formula, which describes the approximate development of binding energies throughout the nuclear chart.

An improvement of the liquid drop model is the droplet model[MS83]. It differentiates between the distribution of protons and neutrons and takes the surface diffuseness into account. It thereby has more parameters and is capable of a more accurate description of nuclear properties like mass (and thereby binding energy) and radial moments. The necessary set of parameters is obtained from a fit to known nuclear properties, as done for example in [BT85]. It is applicable for most of the nuclear chart with generally good agreement. Yet in its simplicity it is incapable of describing, e.g., the distinct drops in binding energy and radii for certain proton or neutron numbers caused by the complex nature of the nucleus. An explanation of these effects requires the nuclear shell model.

2.3.2. Nuclear Shell Model

The particles in the nucleus do not move in a given central potential, as is the case e.g. for the electrons in the atomic shell. Instead the attractive force is caused by interaction among the nucleons. Nevertheless, the fermionic nature of nucleons prevents them from colliding. Thanks to this Pauli-blocking, one can assume that each nucleon is an independent, free particle moving in the mean potential of all the others. If the central potential is chosen carefully, the remaining residual nucleon-nucleon interaction is small and can be treated by perturbation theory. A popular choice is for example the Woods-Saxon-potential [BWW01], which comprises a square well with diffuse surface and is described mathematically by

$$V(r) = -\frac{V_0}{1 + \mathrm{e}^{\frac{r-R}{a}}} \ . \tag{2.23}$$

This approach together with the assumption of a strong spin-orbit coupling in the nucleus leads to single-particle energy levels as depicted in Fig. 2.5, which are filled by neutrons and protons independently. The most important feature of this distribution is the existence of groups of energy levels close to each other with larger shell gaps in between at neutron or proton numbers 2, 8, 20, 28, 50 and 82. As these energy gaps are typically much larger than energies caused by the residual interactions, approaching the shell gap results in filling remaining holes in partially filled shells until they are finally closed, forming a so called "magic" nucleus. Similar to noble gases in atomic physics those nuclei are more stable than surrounding ones. This can be observed for example by looking at binding and excitation energies. Due to the simple symmetry of the closed shells, the remaining residual interaction among nucleons is small and does not distort neither the single particle nature nor the energy levels too much. This allows very accurate predictions with the nuclear shell model in the vicinity of the shell gaps, which is one of the motivations of the investigation of Cd isotopes as performed in this thesis.

Due to the attractive force between nucleons, protons and neutrons usually occupy quantum states with large spatial overlap. Especially the formation of pairs with opposing spin is energetically favored. This can be described by an additional pairing energy. This energy is not constant, but increases with angular momentum of the state [GMJ55]. Depending on the particular size of the effect, the order of energy levels can be different for a single nucleon and for a pair, with high spin states being energetically lower than low spin states for pairs and opposite for single nuclei. Therefore when nucleons are added to a system, e.g. along an isotopic chain, one sometimes can find a given valence nucleon more often than the multiplicity of the shell would allow, as pairs are transferred to a state with higher spin state. Those different states might then be filled without ever accomodating a valence nucleon.

As for paired nucleons the overall spin of the pair as well as induced quantities like magnetic moments cancel out, those properties are zero for even-even nuclei. Furthermore, for odd-even nuclei they are solely determined by the single unpaired valence nucleon.

2.3.3. Magnetic Moments

The magnetic moment is the expectation value of the z-component $\langle I, m = I|\mu_\mathrm{z}|I, m = I\rangle$ of the magnetic dipole operator $\boldsymbol{\mu}$[NN06]. It is related to the spin by $\boldsymbol{\mu_I} = g\mu_N \boldsymbol{I}/\hbar$, where

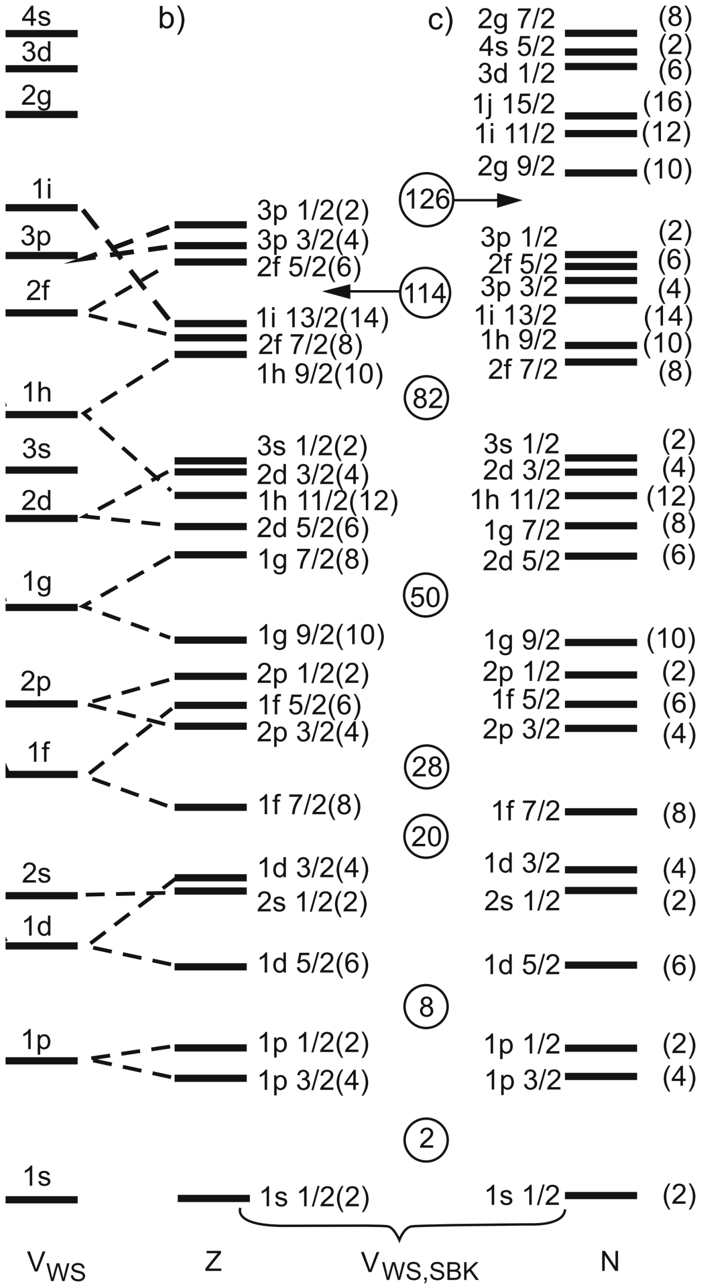
4s
3d
2g
1i
3p
2f
1h
3s
2d
1g
2p
1f
2s
1d
1p
1s
b)
c)
3p 1/2(2)
3p 3/2(4)
2f 5/2(6)
1i 13/2(14)
2f 7/2(8)
1h 9/2(10)
3s 1/2(2)
2d 3/2(4)
1h 11/2(12)
2d 5/2(6)
1g 7/2(8)
1g 9/2(10)
2p 1/2(2)
1f 5/2(6)
2p 3/2(4)
1f 7/2(8)
1d 3/2(4)
2s 1/2(2)
1d 5/2(6)
1p 1/2(2)
1p 3/2(4)
1s 1/2(2)
126
114
82
50
28
20
8
2
2g 7/2 (8)
4s 5/2 (2)
3d 1/2 (6)
1j 15/2 (16)
1i 11/2 (12)
2g 9/2 (10)
3p 1/2 (2)
2f 5/2 (6)
3p 3/2 (4)
1i 13/2 (14)
1h 9/2 (10)
2f 7/2 (8)
3s 1/2 (2)
2d 3/2 (4)
1h 11/2 (12)
1g 7/2 (8)
2d 5/2 (6)
1g 9/2 (10)
2p 1/2 (2)
1f 5/2 (6)
2p 3/2 (4)
1f 7/2 (8)
1d 3/2 (4)
2s 1/2 (2)
1d 5/2 (6)
1p 1/2 (2)
1p 3/2 (4)
1s 1/2 (2)
V_WS
Z
V_WS,SBK
N

Figure 2.5.: Single particle energy levels in the nuclear shell modell for the Wood-Saxon potential without (left) and with spin-orbit coupling for protons (middle) and neutrons (right).[BWW01]

level	$\mu(\nu)$ / μ_N	$\mu(\pi)$ / μ_N
3s 1/2	-1.9	2.8
2d 3/2	1.1	0.1
2d 5/2	-1.9	4.8
1g 7/2	1.5	1.7
1h 11/2	-1.9	7.8

Table 2.1.: Schmidt moments of the nuclear shells between 50 and 82.

μ_N is the nuclear magneton. Due to the pairing of nucleons the magnetic moment of an even number of protons or neutrons does not contribute to the magnetic moment in the nuclear shell model. For odd-even nuclei the magnetic moment is thereby solely determined by the valence nucleon. It consists of two parts originating from spin and orbital angular momentum of the particle

$$\boldsymbol{\mu} = \mu_\mathrm{N} \left(g_l \boldsymbol{l} + g_s \boldsymbol{s} \right) / \hbar \tag{2.24}$$

with the basic g-factors for neutron and proton [NN06]

$$\text{Proton}: \quad g_{\mathrm{p},l} = 1 \quad g_{\mathrm{p},s} = +5.587 \tag{2.25}$$

$$\text{Neutron}: \quad g_{\mathrm{n},l} = 0 \quad g_{\mathrm{n},s} = -3.826\ . \tag{2.26}$$

To obtain the magnetic moment one can calculate the projection onto the quantization axis

$$\boldsymbol{\mu_I} = \frac{\boldsymbol{\mu} \cdot \boldsymbol{I}}{|\boldsymbol{I}|} \cdot \boldsymbol{e_I} = g_{\boldsymbol{I}} \mu_\mathrm{N} \boldsymbol{I} / \hbar \tag{2.27}$$

which leads to

$$\mu_I = \left[\left(I - \frac{1}{2} \right) g_l + \frac{1}{2} g_s \right] \mu_\mathrm{N} \quad \text{for} \quad I = l + \frac{1}{2} \tag{2.28}$$

$$\mu_I = \frac{I}{I+1} \left[\left(I + \frac{3}{2} \right) g_l - \frac{1}{2} g_s \right] \mu_\mathrm{N} \quad \text{for} \quad I = l - \frac{1}{2}\ . \tag{2.29}$$

These are the so called Schmidt moments. As an example the ones for the shells between 50 and 82 are shown in Tab. 2.1. In the nuclear shell model the magnetic moment is constant for each subshell. This neglects residual nucleon-nucleon interaction and is therefore more precise for lighter nuclei and in the vicinity of closed shells. Additional terms like core-polarization can be added to the theory to accommodate for this deficiency.

2.3.4. Electric Quadrupole Moments

As there is no static electric dipole moment due to symmetry, the leading term of an electric multipole expansion is a nuclear electric quadrupole moment. The according operator is defined as

$$\boldsymbol{Q} = \sum_k e_k \left(3z_k^2 - r_k^2\right) \tag{2.30}$$

in cartesian coordinates and can be expressed with the spherical harmonics as

$$\boldsymbol{Q} = \sqrt{\frac{16\pi}{5}} \sum_k e_k r_k^2 Y_2^0 \left(\theta_k, \phi_k\right) \tag{2.31}$$

with the charge e and the summation over all k nucleons[Ney03].

The experimentally accessible observable is again the expectation value of the z-component $\langle Q_z \rangle$, which is called spectroscopic quadrupole moment and can be expressed by the reduced matrix element using the Wigner-Eckart theorem [Ott89]

$$Q_S = \langle I, m = I | \boldsymbol{Q_z} | I, m = I \rangle = \sqrt{\frac{I(2I-1)}{(I+1)(2I+3)}} \langle I || \boldsymbol{Q_z} || I \rangle \ . \tag{2.32}$$

One can see from the formula that it is zero for nuclei with $I \leq 1/2$.

The quadrupole moment is a valuable tool for the investigation of nuclear deformation. In the so called strong-coupling limit, which can be applied for well deformed nuclei with axial symmetry, the spectroscopic quadrupole moment can be linked to the intrinsic quadrupole moment Q_0 through

$$Q_S = \frac{3K_I^2 - I(I+1)}{(I+1)(2I+3)} Q_0 \ . \tag{2.33}$$

Here, K_I is the projection of the total spin I onto the symmetry axis of the deformed nucleus. The intrinsic quadrupole moment can then again be linked to the nuclear shape in the picture of a rigid body, with negative quadrupole moments for oblate deformation and positive quadrupole moments for prolate deformation. Additionally, the quadrupole moment is linked to the nuclear deformation parameter β_2 by

$$Q_0 = \frac{3}{\sqrt{5\pi}} Z R^2 \beta_2 \left(1 + 0.36\beta_2\right) \tag{2.34}$$

with the radius R as described in the next section.

In the shell model picture the properties are solely determined by the valence nucleons, which reduces the sum over all particles to the sum over all valence nucleons. As free neutrons have no charge, they would not produce any quadrupole moment in this picture. However, empirically this is not the case. Due to particle-particle and particle-core (i.e. core polarization) interaction the valence nucleons influence the distribution of the remaining nucleus including the protons and thereby produce a quadrupole moment beyond their direct impact. This is taken into account by using effective charges e^{eff} for protons and neutrons which are mostly mass dependent and vary between $e^{\text{eff}}_{\pi} \approx 1.3e - 1.6e$ and $e^{\text{eff}}_{\nu} \approx 0.35e - 0.96e$ [NN06]. The quadrupole moment induced by a single particle in the nuclear shell model depends on the angular momentum j of the particle and is given by [GMJ55]

$$Q_{\text{sp}} = -e^{\text{eff}} \frac{2j-1}{2j+2} \langle r_j^2 \rangle \tag{2.35}$$

with the mean square radius $\langle r_j^2 \rangle$ for a particle in the respective orbit. A particle in a state $m_j = j$ has a probability distribution concentrated in the equatorial plane. Thus, it is expected to cause an oblate deformation and therefore a negative quadrupole moment. A hole in this state accordingly creates a prolate deformation, leading to a positive quadrupole moment of the same size. As the different m_j levels of the shell are filled consecutively, the quadrupole moment will develop from Q_{sp} to $-Q_{\text{sp}}$ (which implies from negative to positive values). A detailed calculation leads to a linear dependence on the occupation number λ[GMJ55]

$$Q(\lambda) = Q_{\text{sp}} \left(1 - \frac{2(\lambda - 1)}{2j - 1} \right) \ . \tag{2.36}$$

2.3.5. Nuclear Charge Radii

The size of the nucleus is an important property for understanding nuclear structure. In the liquid drop model the nucleus has a sharp surface and therefore the size can be expressed by the radius. As this model also neglects differences between proton and neutron distribution and assumes incompressibility of nuclear matter, it directly leads to a nuclear radius of

$$R = R_0 A^{1/3} \tag{2.37}$$

with the atomic mass number A and $R_0 = 1.2$ fm. Here, the increase in radius is solely caused by an increase in volume due to the larger number of nucleons. This parametrization is refined in the droplet model. For more realistic models without sharp surface, a measure for the nuclear size is the nuclear mean square charge radius

$$\langle r^2 \rangle = \frac{\int \rho(r) \boldsymbol{r}^2 d\boldsymbol{r}}{Ze} \ . \tag{2.38}$$

It can be seen as the monopole moment of the charge distribution. For a solid sphere the relation to the surface radius is $\langle r^2 \rangle = (3/5)R^2$.

Taking deformation into account, the nucleus can be viewed as a quadrupoloid. This can be expressed with spherical harmonics with a radius depending on the angle by

$$R_D(\theta) = R[1 + \alpha + \beta_2 Y_{20}(\theta)] \ . \tag{2.39}$$

$\alpha = -1/(4\pi)\beta_2^2$ is a compensation term to keep the enclosed volume constant for all deformations. A change in deformation of $\delta\langle\beta_2^2\rangle$ results in a change in the mean square charge radius by

$$\delta\langle r^2\rangle = \frac{5}{4\pi}\langle r^2\rangle\delta\langle\beta_2^2\rangle \ . \tag{2.40}$$

Obviously, the ms charge radius for a given volume is smallest for a spherical nucleus. Furthermore, changes in mean square charge radii which deviate from the expected volume effects can be interpreted as a change in deformation and yield complementary information to the measurement of the quadrupole moment created by the deformed nucleus. It especially enables access to intrinsic deformation even for $I = 0$ nuclei, which do not expose quadrupole moments. A large deviation between β_2 obtained from the HFS and β_2 required to explain the increase in charge radius points towards dynamical deformations caused by an oscillation of the nucleus around an average static deformation.

3. Experiment

3.1. Setup

3.1.1. The Cd-Experiment

The goal of the Cadmium experiment is the investigation and measurement of the isotopic chain from $N = 100$ to $N = 130$ and possibly beyond. In the first part of this experiment a beamtime was used to investigate stable and neutron rich isotopes close to stability up to ^{126}Cd. Spectroscopy has been performed on a transition from a metastable state in a continuous beam of neutral Cd. They were produced at ISOLDE at the general purpose separator (GPS) target station, which allows fast switching between masses and is well suited for isotopes with relatively high yield. The setup as well as the data analysis and results are described in detail in [Fr3]. For simplicity this part of the experiment is further called the atomic run.

For the rest of the isotopes an increase in sensitivity was necessary. This has been mainly achieved by using the radiofrequency quadrupole cooler and buncher (RFQ) ISCOOL for background supression and by probing a strong transition in Cd^+ ions at 214.6 nm. Two further runs have been performed, one for neutron rich and one for neutron deficient isotopes. The experimental setup is described in this chapter.

3.1.2. ISOLDE

The Isotope Separator OnLine DEvice is a radioactive ion beam facility at CERN. The layout is shown in Fig. 3.1. There, short lived nuclei are produced by a pulsed proton beam with 1.4 GeV from the Proton Synchrotron Booster (PSB) impinging on a thick target. Isotopes are created mainly through fragmentation, spallation and fission processes. The target was heated to accelerate the diffusion out of the target material and the effusion through a transfer line into the ionization region. Different combinations of targets and ionization schemes are used to access specific regions of the nuclear chart.

For the run on neutron deficient Cd a molten tin target with a plasma ion source provided a high production yield as well as a high ionization efficiency.

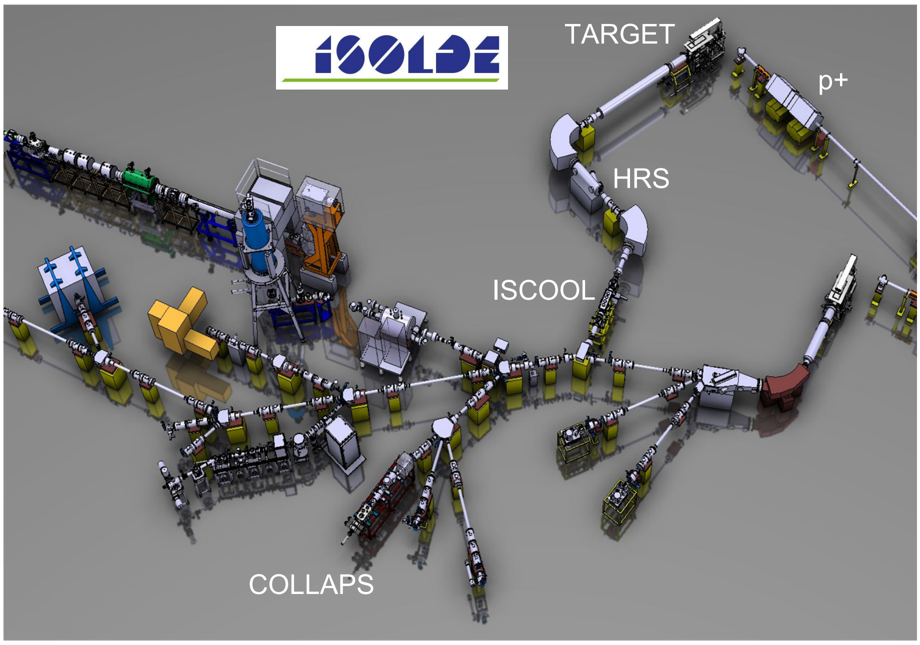

Figure 3.1.: The ISOLDE layout. In this experiment, protons hitting the HRS target station produce radioactive ions which were mass separated, bunched and transported to the COLLAPS aparatus, where spectroscopy was performed. [ISO13]

For the neutron rich isotopes uranium carbide targets provide the highest yield. In this case, beam purity was a main concern as long lived species, especially Cesium, usually have yields that are several orders of magnitude higher. This is particularly a problem since the amount of ions that can be handled by the following RFQ is space charge limited. Several measures have been taken to improve beam purity:

- Instead of bombarding the target with protons, the beam was directed onto a tungsten rod next to the uranium carbide[Cat03]. There, protons are converted into neutrons which then hit the target. Thereby fission becomes the dominating production process. It has a high yield for the desired species, but much less for heavier neutron deficient ones and therefore provides a purer beam, although the overall yield is reduced by a factor of 3–10 due to geometrical constraints.
- Chemical selectivity was added by inserting a quarz tube at lower temperature than the target into the transfer tube [Kt08]. This is isothermal vacuum chromatography, where the chemically highly reactive species like Cs and Rb are retained on the surface of the quartz tube long enough to decay due to their high adsorption enthalpy, while volatile species such as Zn and Cd are not significantly influenced. A suppression of 2–4 orders of magnitude is possible with this approach.

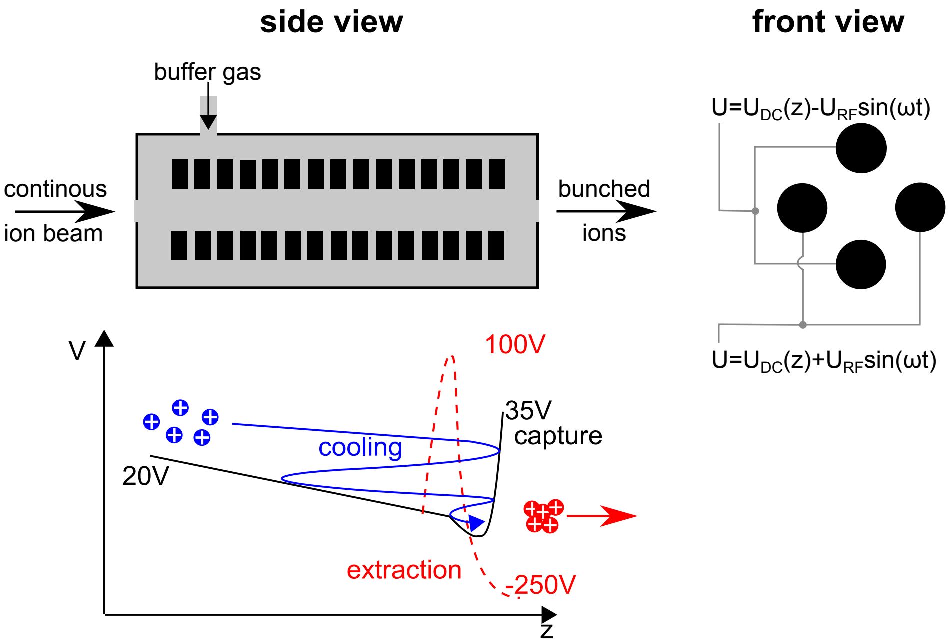

Figure 3.2.: Scheme of the radiofrequency cooler and buncher. Ions are injected into a gas filled linear Paul trap. With the segmented electrodes a longitudinal trapping potential is created, so ions accumulate at the end and thermalize by gas collisions. Afterwards, the end electrode potential is switched down and the ions are extracted as short intense bunch [Gor13].

- The Resonance Ionization Laser Ion Source (RILIS) uses pulsed lasers to selectively ionize a single element by exciting the electron of the atom through several steps into the continuum. For cadmium a three step scheme is used with a resonant first and second step at 228.8 nm and 642.8 nm respectively and a non-resonant third step at 532 nm with an overall efficiency of up to 10%. The laser ionization allows to reduce the source temperature to maintain just a sufficient vapor pressure, thereby reducing the amount of surface ionized contaminants [Kö03].

The ionized particles were extracted and accelerated electrostatically to about 30 keV. Afterwards, they pass the high resolution mass separator (HRS) and were injected into ISCOOL [Man09], a gas filled linear paul trap as shown in Fig. 3.2, which is mounted on a high voltage platform and kept at a potential slightly less than the ion energy. Four metal rods with applied static and radiofrequency voltage potentials create a radial trapping field in the time average. In longitudinal direction the rods are segmented to allow the creation of a potential minimum along this axis for longitudinal trapping as shown in the lower part of Fig. 3.2. High purity Helium is injected into this region with a pressure of about 0.1 mbar. The ions entering the RFQ are slowed down by collisions with the gas and trapped in the potential minimum close to the exit, where they are accumulated over a timespan of about 100 ms and thermalize with the gas. After that, the voltage at the ejection side is lowered and the ions

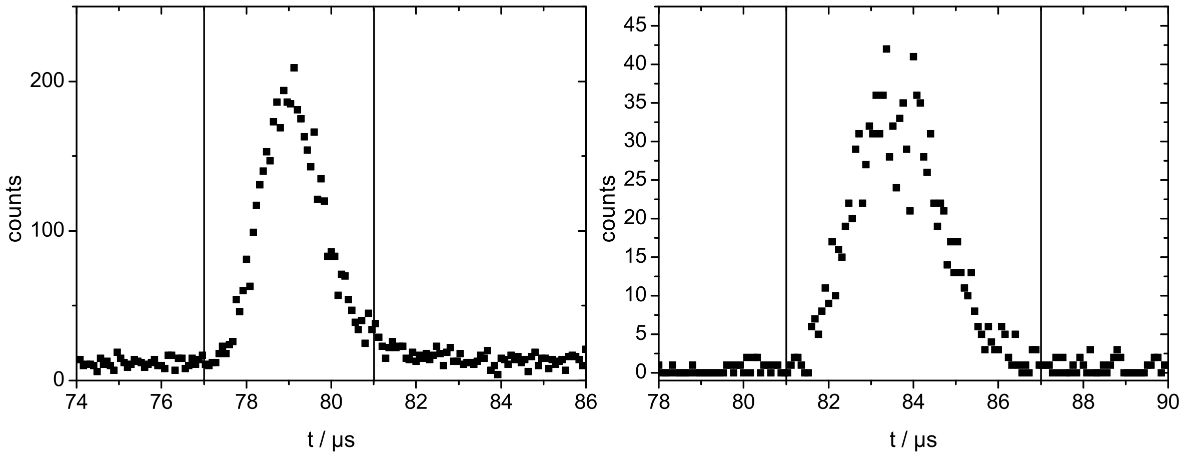

Figure 3.3.: Time of flight spectrum of ^{101}Cd (left) and ^{114}Cd (right) ion bunches measured with the signal from the photomultipliers and a multichannel scaler. The applied coincidence gates are marked inside.

are extracted as a short, intense bunch of some μs, as can be seen in Fig. 3.3. These time of flight spectra were taken for ^{101}Cd and ^{114}Cd during the beamtime. Pulses are 2–4 μs long and by gating the photon detectors on the time window of the passing bunch, the background originating from scattered laser light can be suppressed by a factor of about 10000, given by the ratio of the accumulation time and the length of the time-window. The signal noise is accordingly reduced by the square root of the background reduction (a factor of about 100) without signal loss. The space charge limit of the trap is about 10^6 ions and care has been taken not to exceed this limit by cutting away excess beam for isotopes with high yield.

The cooled and bunched beam was subsequently transported to the beamline of the COLLAPS-experiment.

3.1.3. COLLAPS Beamline

A schematic drawing of the COLLAPS beamline is shown in Fig. 3.4. First, the incoming ion beam passes a 10°-bender, where it is superimposed with the laser beam. Several deflector and quadrupole electrodes are used for fine adjustment of the overlap and collimation of the ion beam. Afterwards, the ion beam enters the detection region, where the scan voltage is applied to change the ion velocity for Doppler tuning. Two sets of two opposing detectors collect the fluorescence photons [Kre13]. Each of them consists of two aspheric 4” lenses in f-f configuration and a photomultiplier tube.

The high voltage is created by a chain of two power supplies. A KEPCO BOP 100 voltage amplifier is capable of scanning very fast across the resonance of each isotope, while a FLUKE 410B high-voltage power supply provides the necessary offset to cover the range necessary for

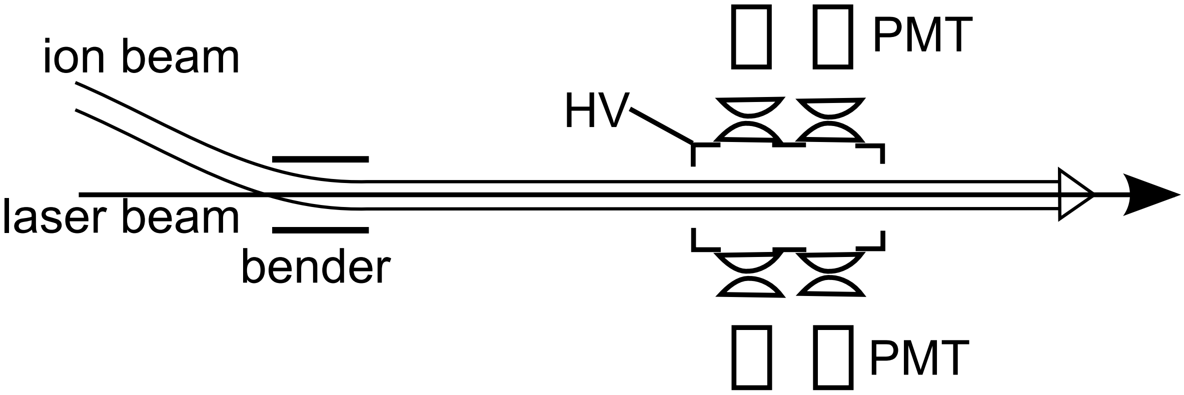

Figure 3.4.: Scheme of the COLLAPS beamline. The ion beam from ISOLDE is overlapped with the laser beam. The optical detection region is on high voltage for post-acceleration. Fluorescence photons are focused by lenses onto the 4 photomultiplier tubes.

all cadmium isotopes. The total voltage can be measured and recorded with a JRL voltage divider and a Prema 6040 digital multimeter.

Several apertures inside the beamline as well as a faraday cup and a multichannel plate detector at the end are used for diagnostics of the spatial distribution, intensity and time structure of the ion beam.

3.1.4. Laser System

A considerable increase in sensitivity compared to the first run on neutral Cadmium arises from the change to the strong $5^2\mathrm{S}_{1/2} \rightarrow 5^2\mathrm{P}_{3/2}$ electric dipole transition in Cd^+, which is shown in the level scheme in Fig. 3.5. Contrary to the atomic spectroscopy no charge exchange for neutralization was necessary and the transition starts from the ground instead of a metastable state, so all ions were available for spectroscopy. An increase in sensitivity by about one order of magnitude was estimated, but it requires the production of 214.6 nm laser light, which is quite demanding. The advantage of the D2 line compared to the D1 line

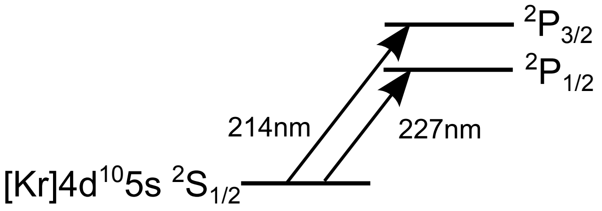

Figure 3.5.: The level scheme of Cadmium. Due to the closed $4d$ subshell it is alkali-like with a closed $5s \rightarrow 5p$ transition.

is the higher spin $J = 3/2$, which allows the observation and determination of spectroscopic quadrupole moments.

To produce laser light of this wavelength, frequency quadruplication of a 859 nm titanium sapphire laser is necessary. This can be achieved by two subsequent second-harmonic generations, which can be explained using nonlinear optics.

Only the first order of the response of the electrons inside the material to the electric field is usually considered for the interaction between light and matter. Hence, the electric polarisation is assumed to be linear in the exciting field

$$\boldsymbol{P} = \epsilon_0 \chi \boldsymbol{E} \ , \tag{3.1}$$

with the complex electric susceptibility χ. This allows the description of absorption and refraction.

While this is accurate for small light intensities, the high electric fields reachable by focused laser light induce additional contributions. This is the field of nonlinear optics, where the interaction is expanded to higher orders according to

$$\boldsymbol{P} = \epsilon_0 \sum_n \chi^n \boldsymbol{E}^n = \epsilon_0 \left(\chi^{(1)} \boldsymbol{E} + \chi^{(2)} \boldsymbol{E}^2 + \chi^{(3)} \boldsymbol{E}^3 + ... \right) \ . \tag{3.2}$$

If excited by an electromagnetic wave of the form

$$\boldsymbol{E}(t) = \boldsymbol{E}_0 (\exp{(i\omega t)} + \exp{(-i\omega t)}) \tag{3.3}$$

the second-order response of the material includes a constant (optical rectification) and oscillations with twice the frequency of the electromagnetic wave[ST07]

$$\boldsymbol{P} = \epsilon_0 \chi^{(2)} \boldsymbol{E}_0^2 (1 + \exp{(i2\omega t)} + \exp{(-i2\omega t)}) \ . \tag{3.4}$$

Without dispersion in the medium, these oscillations would have a well defined phase over the size of the material and therefore an electromagnetic wave with twice the frequency of the exciting fundamental one is generated, the so-called second-harmonic. However, dispersion leads to a rapid decoherence of the waves created at different points and therefore prevents efficient production of higher harmonics. Dispersion compensation, called phase-matching, is usually achieved using birefringent materials. for the so-called critical phase-matching, the optical axis of the crystal is aligned in such a way that the effective refractory index for both frequencies ω and 2ω is identical. This approach is less efficient, but applicable over a large frequency range. For non-critical phase-matching, the crystal is heated to a temperature where dispersion disappears. This yields higher efficiencies, but is not as often applicable because of the limited number of available crystal materials and the wavelength range is additionally restricted since the temperate must lie within reasonable limits.

To achieve high efficiency, a material with a large nonlinear susceptibility $\chi^{(2)}$ has to be chosen. Furthermore, the power of the second-harmonic scales with the square of the fundamental power. As the $\chi^{(2)}$ of even the best crystal is still quite small, continuous wave lasers, even with powers of several watts, require enhancement cavities to achieve a conversion efficiency of several 10 percent. There, the laser light is coupled into a stabilized optical resonator with a nonlinear crystal positioned in the focal plane inside, which leads to power densities about 150 times larger than without the cavity.

As a consequence, frequency quadrupling of a continuous wave laser beam requires two enhancement cavities, one for each second-harmonic generation. In our setup a Verdi-V18 diode-pumped Nd:YAG laser doubled to 532 nm was used to pump a Sirah Matisse TS Titanium:Sapphire ring laser. The laser frequency was measured with a Bristol Instruments 621 Series wavemeter and stabilized to a stable helium neon laser via a transfer cavity. The main part of the laser output was coupled into the cavity of a Tekhnoscan FD-SF-07 frequency doubler. To achieve high coupling efficiencies and thereby high internal power densities, the laser beam has to be manipulated using optical units to exhibit the same focal parameters as the eigenmode of the resonator. This is called mode matching and is critical in achieving reasonable second-harmonic generation efficiencies. Inside the enhancement cavity, whith a length actively stabilized by a Haensch-Coulliaud lock to match the laser wavelength, the second-harmonic at 430 nm was generated in a lithium triborate (LBO) crystal. The resulting elliptic output beam has been collimated with two cylindrical lenses and was subsequently mode matched into a second frequency doubler, a Pound-Drever-Hall locked Spectra-Physics Wavetrain. Using a barium borate (BBO) crystal the frequency was doubled once more to reach the desired wavelength of 214.6 nm. The generated fourth-harmonic radiation was collimated using a cylindrical lens, an anamorph prism pair and a telescope and subsequently transported to the COLLAPS experiment 15 m away, where it was coupled through the beamline after passing a mode cleaner and an exchangable degrader for final power adjustment. A scheme of the setup with all information about the lens assembly is shown in Fig. 3.6 and a photograph in Fig. 3.7.

Typical laser powers during the experiment were 1.2 W from the Ti:Saph, 260 mW after the first doubler and 5 mW after the second doubler, leading to an overall quadrupling efficiency of about 0.5%. This is close to the performance reached for this power during development and commissioning tests in Mainz, as can be seen in Fig. 3.8. Spectroscopy itself was performed with 100-500 μW to limit the influence of optical pumping.

The stability of the laser system was very high during the beamtime. The stabilizations worked well and relocking was necessary only a couple of times during the runs. Unfortunately, the crystal for 215 nm degraded fast at the spot where the laser passed, resulting in diminishing

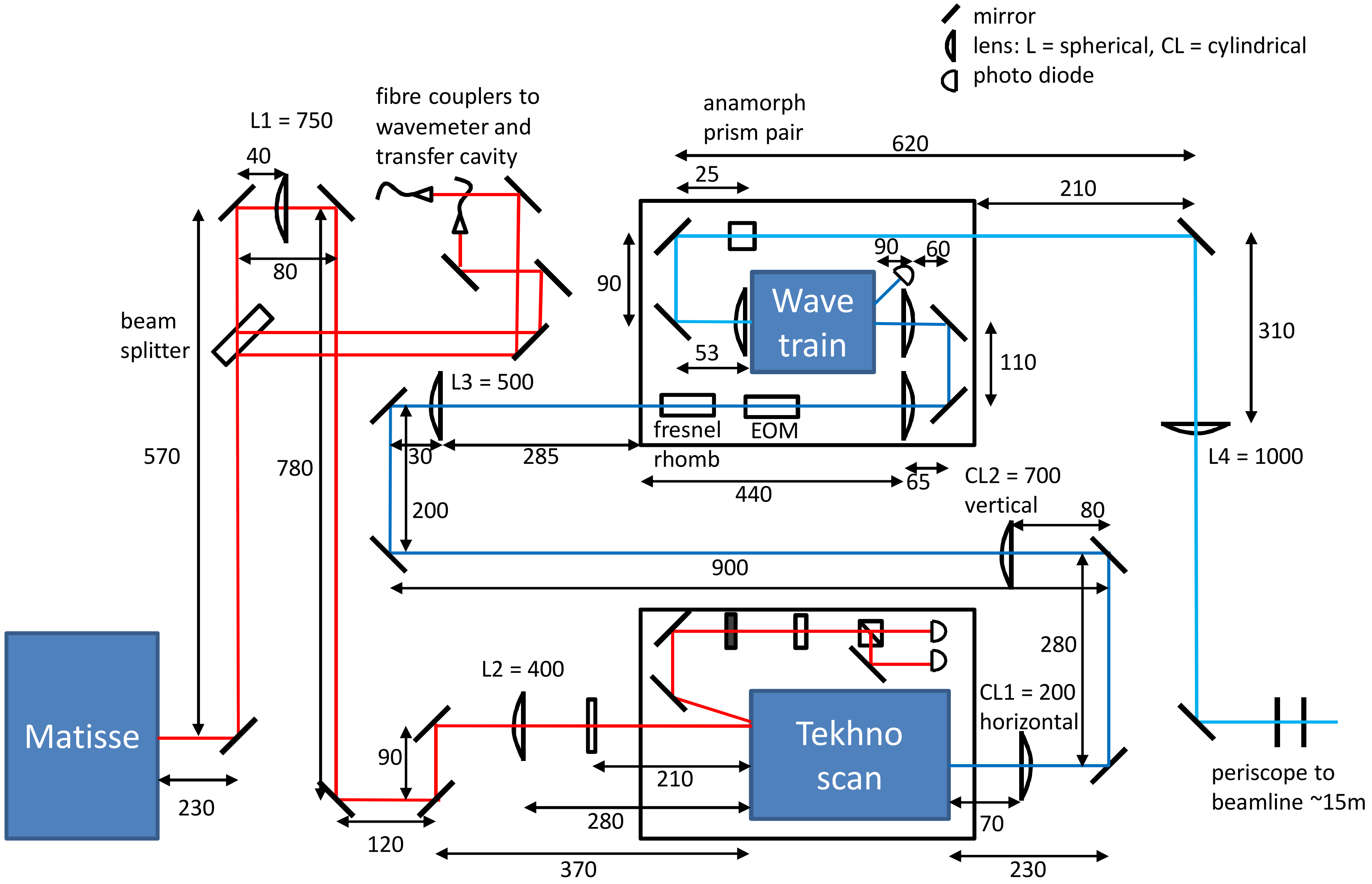
mirror
lens: L = spherical, CL = cylindrical
photo diode
L1 = 750
40
80
fibre couplers to
wavemeter and
transfer cavity
anamorph
prism pair
620
25
210
90
Wave
train
90
60
53
110
310
beam
splitter
570
780
L3 = 500
30
285
200
fresnel
rhomb
EOM
440
65
CL2 = 700
vertical
80
L4 = 1000
900
Matisse
230
90
120
L2 = 400
210
280
370
Tekhno
scan
280
CL1 = 200
horizontal
70
230
periscope to
beamline ~15m

Figure 3.6.: Laser setup for the production of continuous wave laser light at 215 nm by frequency quadrupling. The sketch shows the two consecutive commercial frequency doublers and the modematching optics used. All distances are in mm.

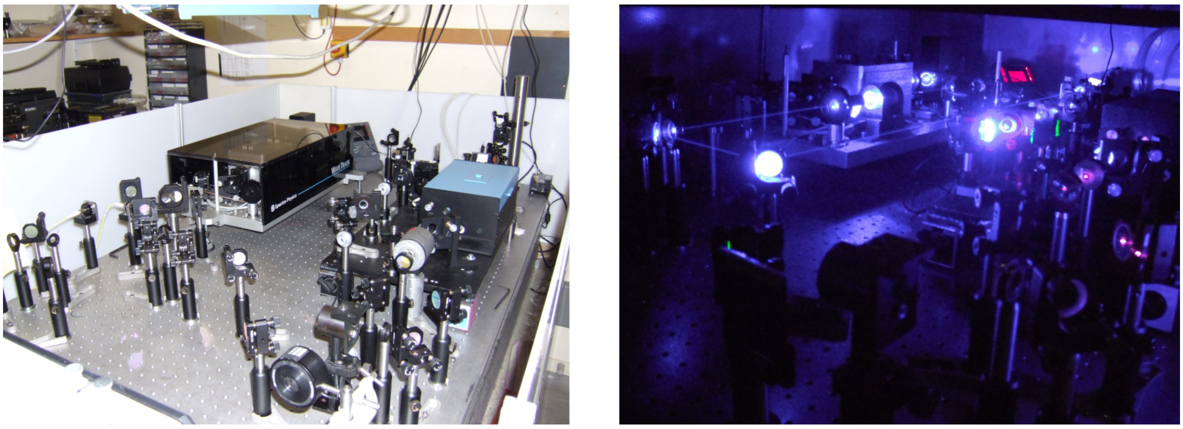

Figure 3.7.: Picture of the frequency quadrupling setup by light and in the dark. In the lower left is the Ti:Saph laser, on the right the first doubler and in the back the second one. Only the second-harmonic laser light of 430 nm is visible.

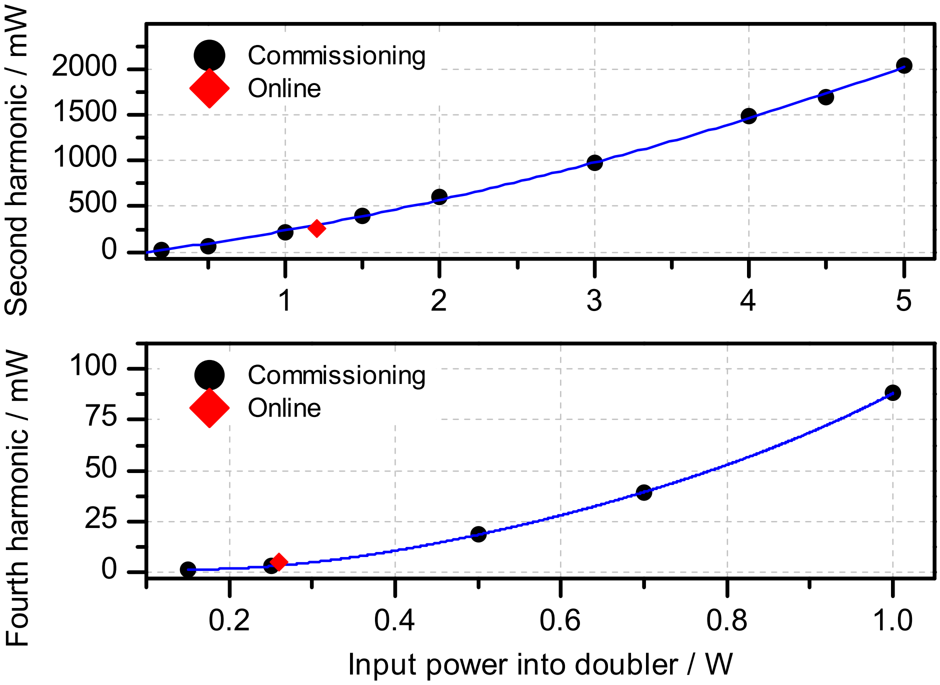

Figure 3.8.: Higher harmonic generation efficiency of the setup during commissioning in black [Kri12] and during the online run in red with fourth order polinomial fit in blue.

doubling efficiencies after about 2 days. Therefore, it had to be translated horizontally several times during the beamtime to retain sufficient laser power for spectroscopy. A second crystal was used during the second run, exhibiting the same behaviour. As this never occured during the several months of commissioning, it is likely that this was caused by the less than optimal environmental conditions in the laser laboratory at ISOLDE.

3.1.5. Data Acquisition

The data acquisition logic of the COLLAPS experiment runs on a VME controller. A scheme of the logic layout is shown in Fig. 3.9. It scans the spectrum of the ions several times by adjusting the scanning voltage. Each spectrum may consist of several voltage ranges which are scanned sequentely a specified number of times. This allows skipping of voltages in between hyperfine structure multiplets and accumulating a variable amount of statistics to compensate for differing strengths of the lines. After scanning each voltage range the offset voltage is measured with the digital voltmeter and saved. Additionally, care was taken to have different numbers of pulses in the proton supercycle and voltage steps to average possible yield fluctuations caused by the unregular distribution of protons from the PSB.

From the measured time of flight spectra of the ion bunches a gate including most of the ions was determined for each isotope. With a delay-gate-generator a pulse according to this measurement was produced. The signal from the photomultipliers was discriminated into a digital signal and the coincidence between ion bunch and photons was created by applying a logical AND between the two signals. For each PMT the initial signal as well as the coincidence signal was fed into a scaler. Those scalers were read out and reset for each voltage step.

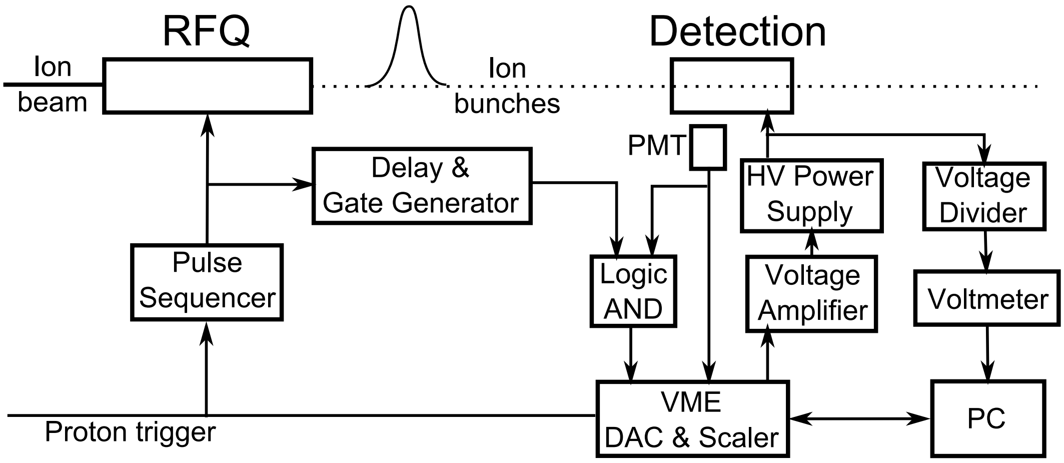

Figure 3.9.: Data acquisition system of COLLAPS as used in this experiment. The RFQ is controlled by a pulse sequencer and the photomultiplier signal is recorded after the coincidence logic. The scan voltage is applied to the detection region through a two stage power supply and measured by a voltage divider and a voltmeter.

Accumulation and ejection of the ion bunches was controlled by a pulse sequence generator. Two basic modes were used. For isotopes with half-lifes longer or in the order of the time between proton pulses, the buncher was running continuously and the scan voltage was incremented one step after a certain amount of bunches. For isotopes with shorter half-lifes, the buncher was triggered by the proton pulse to deliver several bunches depending on the half-life and the scan voltage was incremented after each proton pulse.

4. Analysis and Interpretation

4.1. Fitting the Spectra and Spin Determination

4.1.1. Calculating the Rest Frame Frequency

The data obtained from the experiment include the counts registered in each photomultiplier for every applied scan voltage. To convert the voltage to a rest frame frequency, the velocity has to be calculated from the kinetic energy relativistically and inserted into the doppler formula for collinear geometry between laser and ion beam:

$$v = c \cdot \sqrt{1 - \left(\frac{mc^2}{e\left(U_{\text{source}} - U_{\text{scan}}\right) + mc^2} \right)^2} \tag{4.1}$$

$$\nu = \nu_{\text{Laser}} \cdot \sqrt{\frac{c - v}{c + v}} \ . \tag{4.2}$$

Obviously, additional information is necessary.

The laser frequency ν_{Laser} was logged with a HeNe-stabilized wavemeter with an accuracy of approximately 60 MHz. The measured values are averaged over each beamtime, as it was constant within the accuracy of the wavemeter.

The RFQ voltage U_{source} was measured with a voltage divider and a precision digital multimeter. The result is shown in Fig. 4.1. A relative error of 1×10^{-4} is estimated from calibration measurements of the divider chain, resulting in about 3 V absolute error. During the first run the power supply had to be switched off for a planned maintenance, after which it recovered to almost the same value. It is not possible to tell from this measurement whether it is the power supply or the voltage divider that has to settle afterwards. Therefore for analysis of the data the average of the stable plateau was used (shown in red). During the second run conditions where less stable, but the fluctuations still well within the accuracy of the voltage divider. Therefore again the average of the run has been used for the analysis. The single freak value at the bottom was caused by a power loss.

The offset voltage of the detection region was automatically measured after every track as explained in 3.1. For each scan those values were averaged.

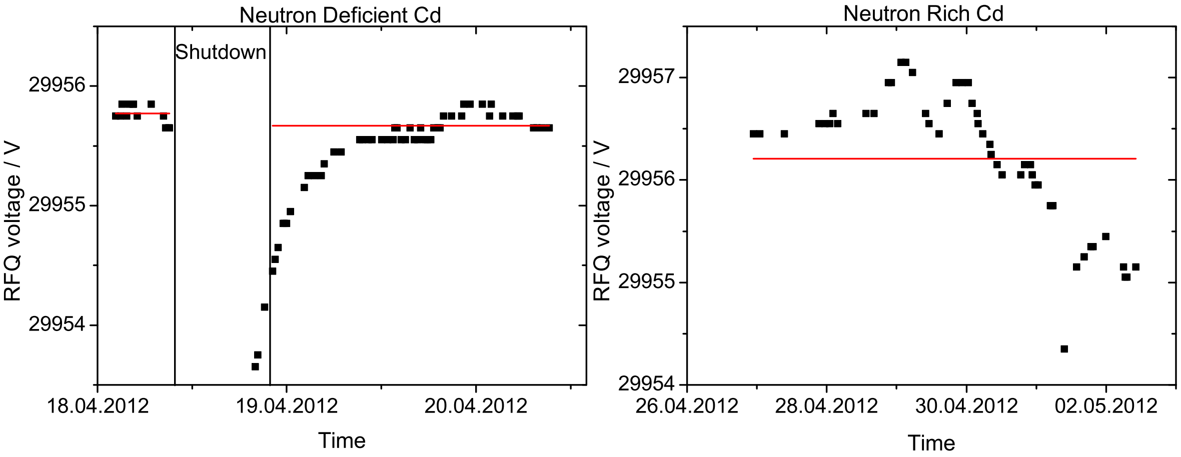

Figure 4.1.: Measured RFQ voltages of the two runs and average values. See text for explanation.

To determine the amplification factor of the scan voltage amplifier, a voltage ramp across the complete operational range of the Kepco-amplifier was applied and for every set value the potential of the detection region was measured with the same high precison voltage divider as the offset voltage. Afterwards a linear function was fitted to this scan. As the results showed no significant variation over a beamtime, the values were averaged with a resulting amplification factor of 100.181(4) and 100.189(3) for the two runs. The relative systematic uncertainty of the voltage divider is 1×10^{-4}. As the two power supplies are connected in a chain it is easy to see that the resulting sum voltage $U_{\text{scan}} = U_{\text{Offset}} + U_{\text{Amplifier}}$ as well as voltage differences have a relative systematic accuracy of 1×10^{-4} as well.

The ion masses required in Eq. 4.1 are taken from AME [WA12] and newer penning trap mass measurements [Kan12] where available as listed in Sec. A.1. For ^{127}Cd and ^{129}Cd, for which neither the isomeric mass nor the spin is known, the mass of the ground state was used and the uncertainty was estimated as the largest excitation energy of the known isomers in the vicinity, namely 300 keV.

With these values the rest frame frequency according to each scanning voltage is calculated and the scale thereby transformed into frequency space.

4.1.2. Uncertainty Estimation of the Number of Counts

The error of the number of counts in each channel has been estimated by the maximum of its square root and 1, to accomodate for the case of zero counts in a channel. This happened off-resonance due to the background suppression by gating on the RFQ bunches, where usually very little events were registered. Although this approach neglects the asymmetric errors predicted by Poisson statistics for numbers below about 8, such low numbers only occur off-

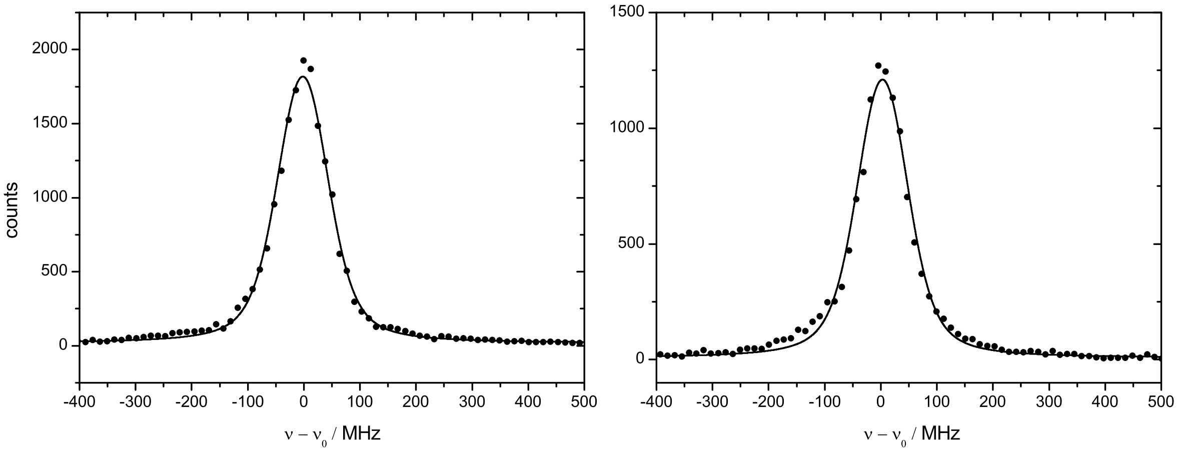

Figure 4.2.: Two spectra of ^{114}Cd. The voigt describes the lineshape quite well. Some spectra, one of them shown on the right, show a small shoulder on the low frequency side.

resonance and thus only have impact on the – in this experiment irrelevant – background rate. For the determination of the line center, which is the required physical property to be extracted, the approximation is sufficient and symmetric errors simplify the fitting procedure.

To accomodate cases with different measurement times on the tracks within a scan, the count rates as well as the errors have been scaled by the respective ratio.

4.1.3. Lineshape Determination

For fitting the Minuit2 package included in root was used. First, using the large amount of scans of the stable reference ^{114}Cd, which has a nuclear spin of $I = 0$ and therefore only one transition in its hyperfine structure, the agreement in line center between the four photomultipliers was confirmed. This allows to sum the counts of all of them to increase the signal-to-noise ratio. Next the lineshape has to be determined to accurately extract the parameters from the fit, especially for exotic isotopes for which the statistics is insufficient for a large amount of free parameters. As described in 2.1, from atomic theory a voigt-profile with the natural linewidth of 44.56 MHz [NIS12] as lorenzian part is expected under the assumption of a gaussian velocity spread and neglectable power broadening. Fixing the according parameter results in an average gaussian contribution of 33.4 MHz and 35.2 MHz, obtained from the reference scans of the neutron deficient and neutron rich run respectively. The gaussian width parameter is fixed for all further fits as well. The resulting lineshape agrees quite well with our observation, although in some spectra a small shoulder at the low frequency side is visible as can be seen in Fig. 4.2. The influence on the extracted properties of this is neglectable, since isotope shifts are evaluated and the lineshapes of the reference isotope and the exotic one were similar in all cases.

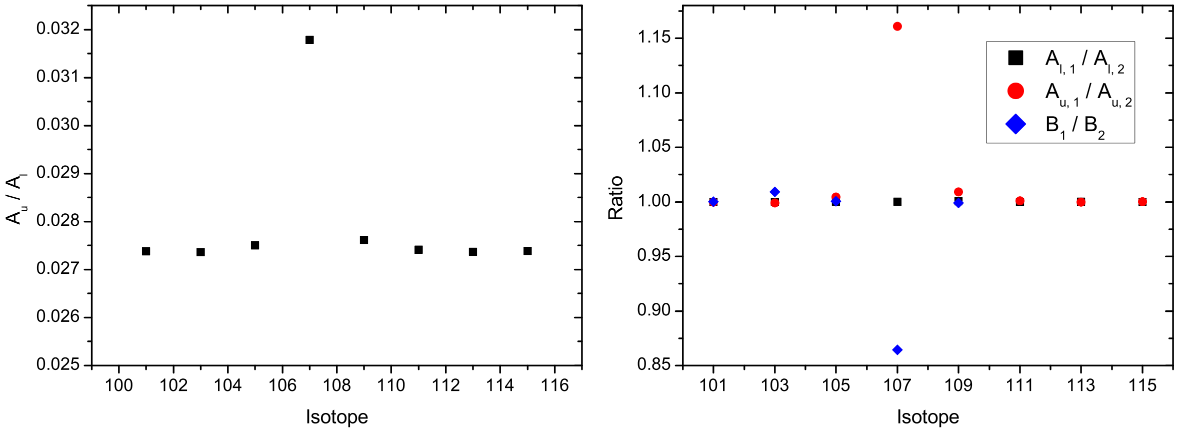

Figure 4.3.: The result of hyperfine structure fits with free A-factor ratio (left) shows an unphysically strong deviation around ^{107}Cd caused by correlation with the B-factor. Fixing the A-factor ratio to the average of stable, odd Cd isotopes does not influence the lower A-factor but resolves the issue. This can be seen on the right, where the ratio of the A- and B-factors obtained with free A-factor ratio (analysis 1) and fixed A-factor ratio (analysis 2) is shown.

The hyperfine spectrum of each isotope is calculated using the selection rules from nuclear and atomic angular momentum. The positions of the N allowed lines relative to the center of gravity can be calculated from A- and B-factors. The final spectrum is the sum of a voigt profile at every line position. As starting parameter for the peak heights relative intensities are calculated using the racah coefficients. Due to optical pumping relative line intensities deviate visibly from the theoretical values, an effect which depends on the laser power used for probing the transition. Such a hyperfine spectrum has up to $4 + N$ free parameters, namely center of gravity, upper and lower A-factor, upper B-factor and the intensity of each transition. If an isomeric state is present, the sum of the two structures is fitted simultaneously.

4.1.4. A-ratio and Hyperfine Anomaly

From the stable, odd Cd isotopes the ratio of upper and lower A-factor can be extracted. In this transition it is $A_{up}/A_{low} = 0.02738(3)$. The small A-factor ratio leads to hyperfine spectra with widely spaced multiplets of lines. The relative accuracy of the lower state splitting is much higher. According to atomic theory the A-factor ratio is almost constant between different isotopes. Only small differences in the distribution of the magnetic moment lead to the so called hyperfine anomaly, an effect usually smaller than one percent. As this is less than the accuracy in the upper A-factor, it is not observable in our experiment. Furthermore, fitting of the light isotopes reveals a strong deviation of the A-factor ratio around ^{107}Cd as shown in Fig. 4.3 on the left, which can not be explained by any physical effect. Fitting the same data a second time with fixed A-factor ratio does not influence the lower A-factor, but leads to a change of the B-factor of ^{107}Cd by avout 15% as shown on the right side

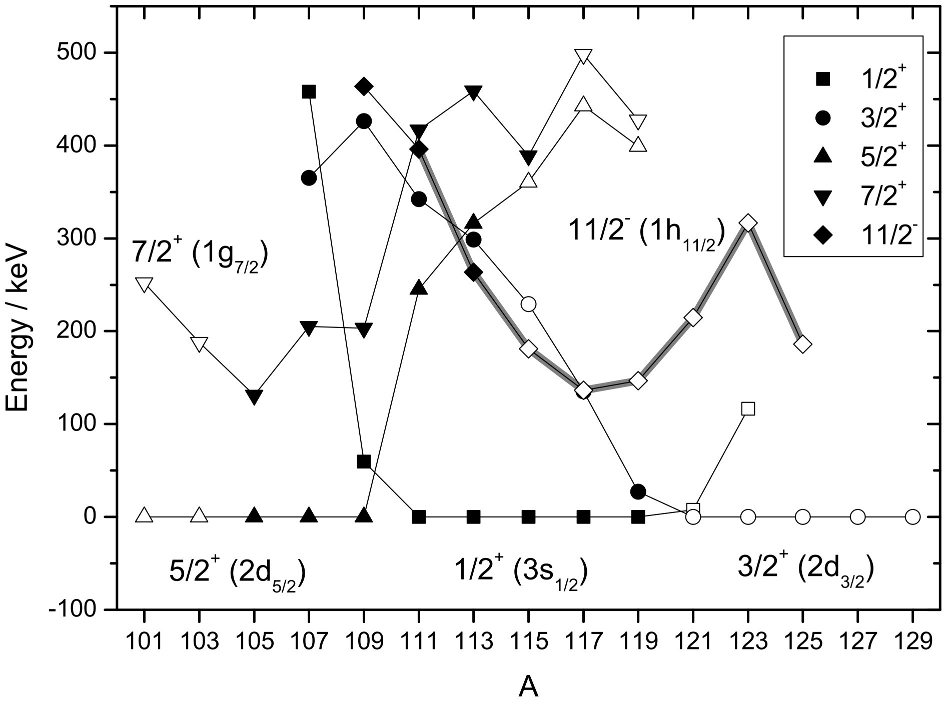

Figure 4.4.: Energy levels of odd-A Cd isotopes relative to the ground state. Spins only tentatively assigned before this work are represented by open symbols. The isomeric state is marked grey. [Nat13]

in Fig. 4.3. This indicates a strong correlation between upper A- and B-factor, leading to inaccurate results. This is supported as well by known quadrupole moments, which favor the B-factors extracted from the analysis with fixed A-factor ratio as will be explained in the according section. Therefore, the latter approach was chosen for this data analysis, reducing the number of free parameters by one. The handling of the hyperfine anomaly in respect to the extraction of the magnetic moments is discussed in section 4.2.

4.1.5. Spin Determination and Identification

The ground state of all even Cd isotopes has nuclear spin zero and thereby no hyperfine structure. For the odd isotopes close to stability the nuclear spin is known, for the ground as well as for the isomeric state, the others were only tentatively assigned previous to this work. The energy levels are plotted in Fig. 4.4 and show the transition of the ground state of the valence neutron between the 5/2, 1/2 and 3/2 shells. In the $5^2\mathrm{S}_{1/2} \rightarrow 5^2\mathrm{P}_{3/2}$ transition under study nuclear spins of $I = 0$ and $I = 1/2$ can be assigned unambiguously by the number of components in the hyperfine spectrum, which is one or three respectively. For a nuclear spin of $I = 3/2$ and above, the number of components is limited to six by the J of the upper electronic state, resulting in two multiplets with 3 lines each. Since relative intensities for different nuclear spins calculated from the racah coefficients are very similar and the observed ratios are altered by optical pumping, a spin assignment based on those observables is not reliable. Instead, the development of the spectra along the chain can be investigated. This allows to distinguish between $I = 11/2$ and $I = 1/2$ and $I = 3/2$ further away from stability. To demonstrate this, spectra from ^{119}Cd, ^{121}Cd and ^{127}Cd are shown in Fig. 4.5. Since mass or excitation energy of a nuclear state can not be extracted from laser spectroscopy, it is not possible to determine which state is the ground state and which one the isomer beyond ^{125}Cd. The same continuity of the development suggests that the spin does not change from ^{109}Cd to ^{101}Cd and is therefore 5/2. This goes as well for the high-spin state from ^{111m}Cd to ^{129m}Cd and the 3/2 state from ^{121}Cd to ^{129}Cd, which was firmly assigned for the first two odd isotopes of the row in the atomic run [Fr3].

Those spin assignments are also strongly supported by the resulting magnetic moments, which are discussed in the next section.

4.1.6. ^{129}Cd

The yield of ^{129}Cd is very low and the hyperfine structure decreases sensitivity further by reducing the population in each hyperfine state as well as the average number of transitions in a single ion due to optical pumping. This results in overall smaller peaks. For accurate determination of A- and B-factors at least three lines have to be measured, for good accuracy all six are necessary. Hence, one has to scan a large area and gather sufficient statistics to see even the smallest peak, making this isotope even harder to investigate than ^{130}Cd. Additionally, in ^{129}Cd the left multiplets of ground and isomeric state collide as plotted in Fig. 4.6 at the bottom, obscuring the structure which even leads to unphysical negative peaks as fit result, clearly impeding the accuracy. To counter this, the spectra have been fitted with relative peak intensities fixed to the average of ^{125}Cd and ^{125m}Cd, respectively, where all peaks are resolved and similar laser power was used as can be seen in Fig. 4.6 at the top. This enhances the fit result and gives more plausible values. To account for the uncertainty introduced by fixing parameters to experimentally determined values, half of the shift induced by fixing them is added quadratically to the error of the extracted results after averaging as described below.

4.2. Moments

For the final determination of a single set of A- and B-factors, all measurements of one isotope are averaged weighted with the statistical error of the fit. The maximum of the propagated error and the standard error of the mean of the sample is used as statistical error. Comparison with an independent analysis with different lineshape, A-ratio and averaging procedure shows a mean difference of 1.3 MHz and 3 MHz for A- and B-factor respectively [Yor13c], which is

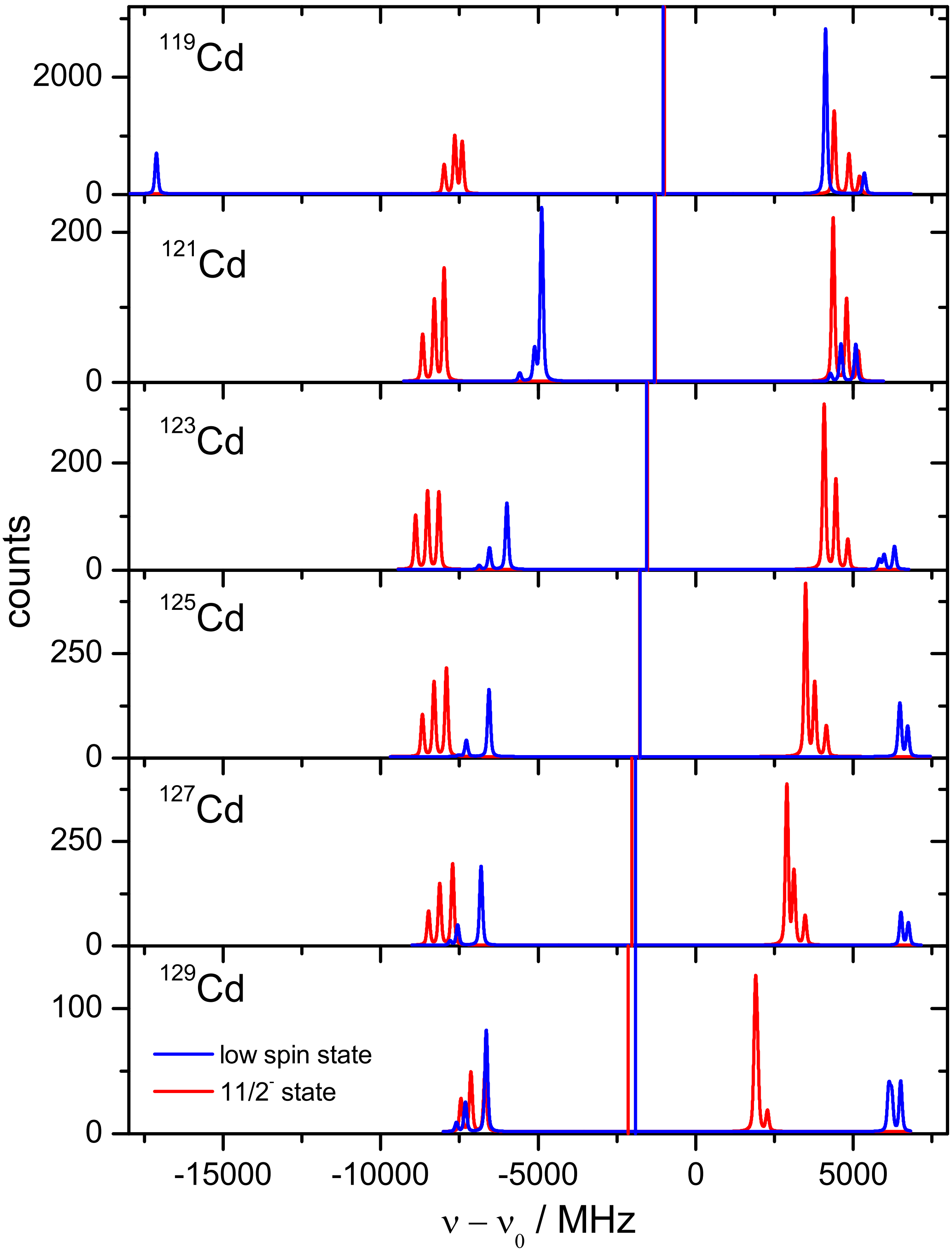

Figure 4.5.: Fitted spectra of odd cadmium isotopes from $A = 119$ to $A = 129$. Vertical lines mark the center of gravity of the hyperfine structures. One can clearly see the spin change from $I = 1/2$ to $I = 3/2$ in the ground state between ^{119}Cd and ^{121}Cd. Other than that, the spectra are very continuous. The dominant changes are the isotope shift and the change in A-factor.

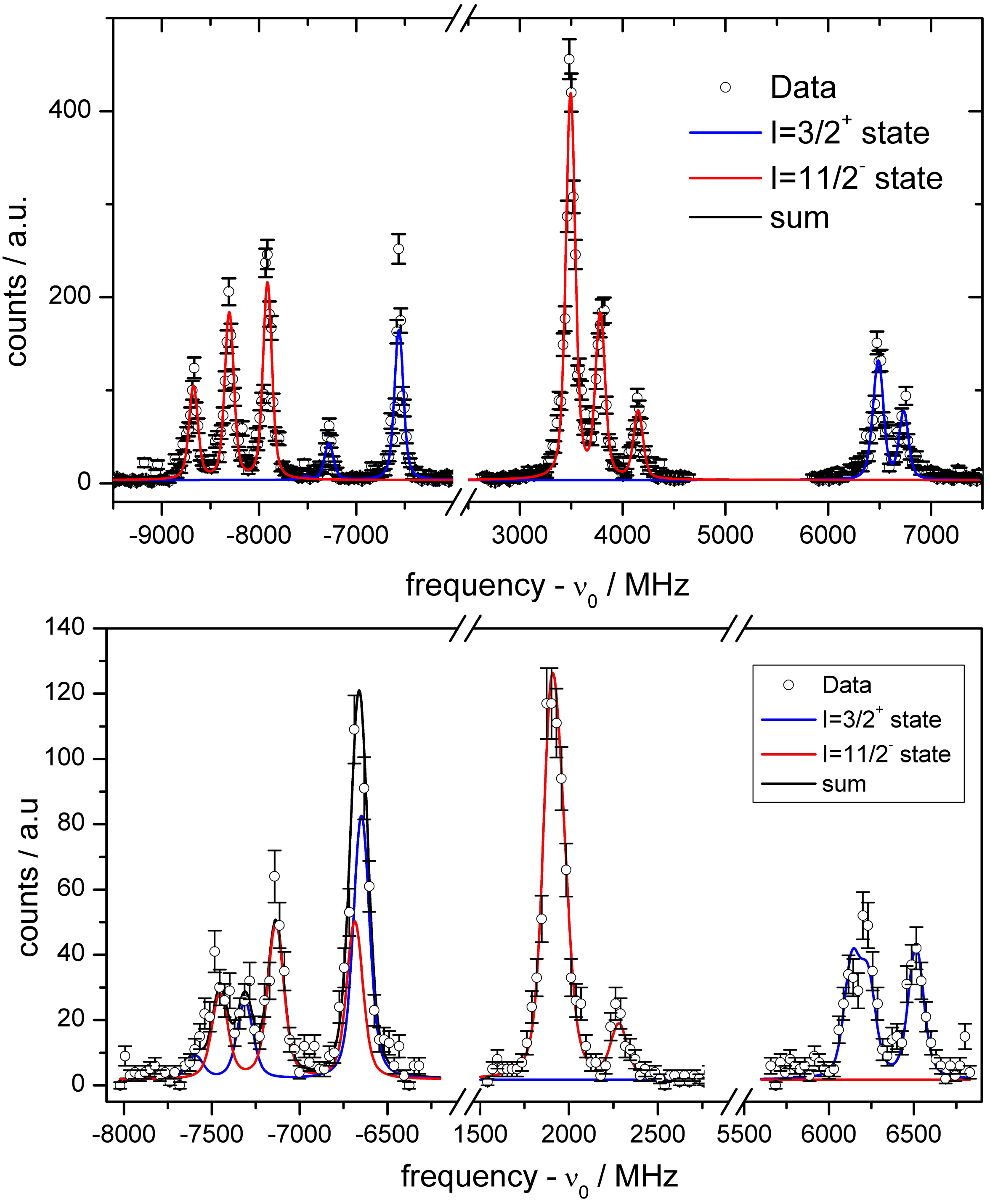

Figure 4.6.: Spectra of ^{125}Cd (top) and ^{129}Cd (bottom). The relative line intensities from the former isotope are used for fitting the latter to limit the loss of accuracy due to the collision of the left multiplets.

added to the error quadratically to reflect the influence of choices made during analysis on the resulting parameters.

As the determination of A- and B-factors happens basically from voltage differences within one scan, the systematic uncertainties are dominated by the accuracy with which those can be measured. Thereby, the relative systematic error is the same as for the scan voltage. The results are summarized in Tab. 4.1 and Tab. 4.2.

4.2.1. Magnetic Moment

As explained in 2.1, the A-factor is linked to the magnetic moment by $A = g_I \mu_N B(0) = \mu_I B(0)/I$. Without knowledge of the local magnetic field $B(0)$, only the ratio of magnetic moments between isotopes can be determined. Using reference values available for stable isotopes from NMR measurements, which have much higher precision than those from laser spectroscopy, absolute moments can be calculated according to

$$\mu = A \cdot \frac{\mu_{\mathrm{ref}}}{A_{\mathrm{ref}}} \,. \tag{4.3}$$

Additionally, the ratio A/A_{ref} is insensitive to systematic errors, because they cancel as they are linear in A. The remaining errors are the statistical errors of the magnetic coupling constant and of the reference magnetic moment as systematic error, where the latter is neglectable due to the high precision of the NMR measurements.

It is observed that the literature values are well reproduced if a reference isotope with the same spin as the isotope under investigation is chosen, but a systematic deviation occurs if all isotopes are referenced to the same isotope regardless of their spin. The largest deviation is found between the 1/2 and 5/2 isotopes, where $1 - (A_{1/2}/A_{3/2})/(\mu_{1/2}/\mu_{3/2}) = 1.1 \cdot 10^{-3}$. This behaviour can be explained by different distributions of magnetization in nuclei with different spin. This is called hyperfine anomaly and alters Eq. 4.3. It is assumed that the hyperfine anomaly can be neglected within each set of isotopes with equal spin, which is supported by the comparison with the known magnetic moments. While reference isotopes exist for the spin values 1/2, 5/2 and 11/2, there is no reference moment for the $I = 3/2$ isotopes. Here ^{111}Cd has been used as reference and the largest observed hyperfine anomaly as stated above has been added as relative systematic error.

The measured magnetic moments agree well with the literature data as well as with the moments derived from the atomic transition. A comparison is plotted in the appendix. A.2.

The magnetic moments reproduce the sign expected from the Schmidt moments, but are about 40-50% smaller than predicted by the single particle levels, which is not uncommon. Usually one would expect the moments to develop towards the single particle predictions as

$Z + N$	I	A_l / MHz	μ / μ_N	μ_Atom / μ_N	μ_Lit / μ_N
101	5/2	-4395.6(14)[05]	-0.8985(3)[00]		
103	5/2	-4158.2(13)[05]	-0.8500(3)[00]		-0.8100000(300000)
105	5/2	-3615.7(14)[04]	-0.7391(3)[00]		-0.7393000(002000)
107	5/2	-3009.1(14)[03]	-0.6151(3)[00]	-0.6154(3)	-0.6150554(000011)
*109	5/2	-4049.9(13)[05]			-0.8278461(000015)
*111	1/2	-14535.9(27)[16]			-0.5948861(000008)
113	1/2	-15204.7(18)[17]	-0.6223(1)[00]	-0.6224(1)	-0.6223009(000009)
115	1/2	-15839.6(37)[18]	-0.6482(2)[00]	-0.6483(1)	-0.6484259(000012)
117	1/2	-18166.2(36)[20]	-0.7435(2)[00]	-0.7437(1)	
119	1/2	-22483.6(29)[25]	-0.9201(2)[00]	-0.9199(2)	
121	3/2	5101.4(47)[06]	0.6263(6)[08]	0.6268(11)	
123	3/2	6434.1(36)[07]	0.7900(5)[10]	0.7900(14)	
125	3/2	7012.0(37)[08]	0.8609(5)[11]		
127	3/2	7158.9(43)[08]	0.8789(6)[11]		
129	3/2	6916.9(55)[08]	0.8492(7)[11]		
111	11/2	-2456.5(13)[03]	-1.1049(8)[00]	-1.1052(4)	-1.1051000(004000)
*113	11/2	-2418.5(13)[03]		-1.0877(4)	-1.0877840(000020)
115	11/2	-2313.4(14)[03]	-1.0405(8)[00]		-1.0410343(000015)
117	11/2	-2217.2(15)[02]	-0.9972(9)[00]	-0.9969(4)	
119	11/2	-2142.5(13)[02]	-0.9637(8)[00]	-0.9636(5)	
121	11/2	-2243.9(15)[03]	-1.0093(9)[00]	-1.0098(5)	
123	11/2	-2224.9(14)[02]	-1.0007(8)[00]	-1.0008(6)	
125	11/2	-2077.7(14)[02]	-0.9345(8)[00]		
127	11/2	-1934.5(13)[02]	-0.8701(8)[00]		
129	11/2	-1569.1(18)[02]	-0.7057(9)[00]		

Table 4.1.: Measured A-factors of the ionic ground state and derived magnetic moments μ. Round brackets enclose the statistic, square brackets the systematic uncertainties. Magnetic moments from the atomic run and from literature [Sto05] are shown as well, the isotopes used as reference for the according spin are marked by an asterisk. ^{111}Cd is used as reference for the spin 3/2 isotopes and the uncertainty due to the hyperfine anomaly is added as systematic error as explained in the text.

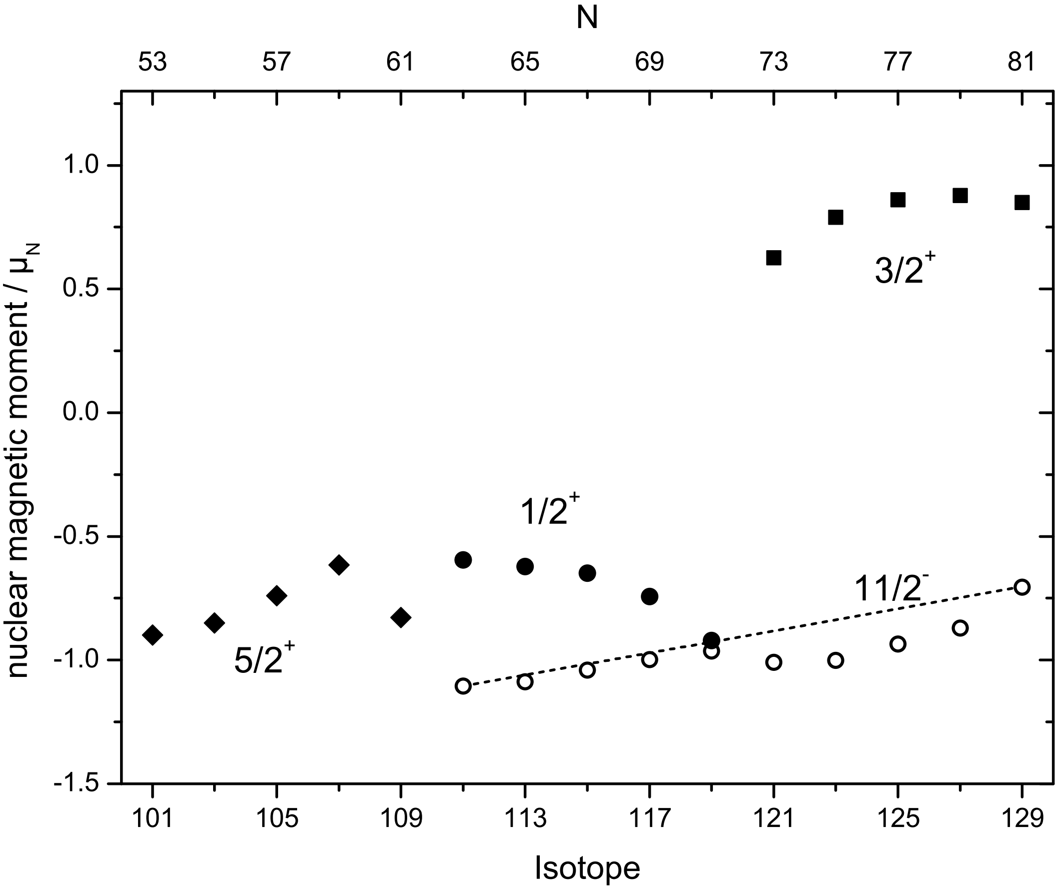

Figure 4.7.: Magnetic moments of the Cd isotopic chain. The values are about 40-50% smaller than the single-particle Schmidt values, which is not uncommon.

they come closer to the shell gap, since core polarizability is reduced by the lack of particles. This is not observed in Cd, where the magnetic moment of ^{129}Cd is further away from the single particle values than ^{127}Cd and ^{125}Cd. This could be caused by the missing proton pair, leading to stronger residual interaction in those nuclei. Another observation is the linear trend in the lower half of the 11/2 shell and the small difference of the magnetic moments in the 11/2 and the ground state before the spin change in the ground state at ^{119}Cd. After this happens, the linear trend of the $I = 11/2$ moments is altered for several isotopes, until it is restored at ^{129}Cd.

4.2.2. Quadrupole Moment

The quadrupole moment is linked to the B-factor by $B = eQ\langle V_{zz}\rangle$. To extract it, one needs either a reference value for one isotope or knowledge of the hyperfine field created by the electron shell. Since a technique to measure quadrupole moments of stable nuclei with

A	I)	B / MHz	Q / b	Q_{Atom} / b	Q_{Lit} / b
101	5/2	-117.3(034)[0]	-0.176(05)[07]		
103	5/2	-3.4(035)[0]	-0.005(05)[00]		-0.80(70)
105	5/2	250.2(032)[0]	0.376(05)[15]		0.43(04)
107	5/2	398.6(033)[0]	0.599(05)[24]	0.593(07)[25]	0.68(07)
109	5/2	399.9(031)[0]	0.600(05)[24]	0.604(04)[25]	0.69(07)
121	3/2	-191.8(086)[0]	-0.288(13)[12]	-0.288(15)[12]	
123	3/2	28.6(060)[0]	0.043(09)[02]	0.063(07)[03]	
125	3/2	144.6(068)[0]	0.217(10)[09]		
127	3/2	158.5(082)[0]	0.238(12)[10]		
129	3/2	93.0(052)[0]	0.140(08)[06]		
111	11/2	-489.1(036)[1]	-0.734(05)[30]	-0.742(05)[31]	-0.85(09)
113	11/2	-405.2(034)[0]	-0.608(05)[25]	-0.612(04)[25]	-0.71(07)
115	11/2	-314.1(047)[0]	-0.472(07)[19]	-0.478(04)[20]	-0.54(05)
117	11/2	-212.1(066)[0]	-0.318(10)[13]	-0.319(02)[13]	
119	11/2	-90.9(039)[0]	-0.136(06)[06]	-0.136(03)[06]	
121	11/2	5.9(066)[0]	0.009(10)[00]	0.007(06)[00]	
123	11/2	88.2(056)[0]	0.132(08)[05]	0.128(11)[05]	
125	11/2	178.5(049)[0]	0.268(07)[11]		
127	11/2	224.9(064)[0]	0.338(10)[14]		
129	11/2	369.1(105)[0]	0.554(16)[22]		

Table 4.2.: Measured B-factors and derived quadrupole moments Q evaluated with $\langle V_{zz}\rangle =$ 666(27) MHz/b [BF13] obtained from Dirac-Hartree-Fock calculations using the GRASP code [Jt13]. Literature values are taken from [Sto05].

similar precision as it is possible for magnetic moments is not available, we use a theory value of

$$\frac{\partial^2 V}{\partial z^2} = 666(27)\mathrm{MHz} \ / \ \mathrm{b} \ , \tag{4.4}$$

calculated by S. Fritzsche and J. Bieroń [BF13]. The value is obtained from Dirac-Hartree-Fock calculations [Gra94] utilizing the atomic structure code GRASP [Jt07][Jt13]. The final result is shown in Tab 4.2. The statistical error is propagated from the electric coupling constant, while the systematic error is dominated by the 4% uncertainty of the theory value.

Although the relative quadrupole moments of our measurement agree very well with the literature data, the absolute values are about 15% smaller. This can be attributed to a different value for V_{zz} of the literature moments. The agreement with the quadrupole moments obtained from spectroscopy of the atomic transition [Fr3] is good as shown in Sec. A.2.

The most striking observation of the measured quadrupole moments is the extremely linear trend in the $I = 11/2$ state with a zero-crossing around ^{121}Cd, plotted in detail in Fig. 4.9 on the left. This is exactly the behaviour expected from simple shell model single-particle

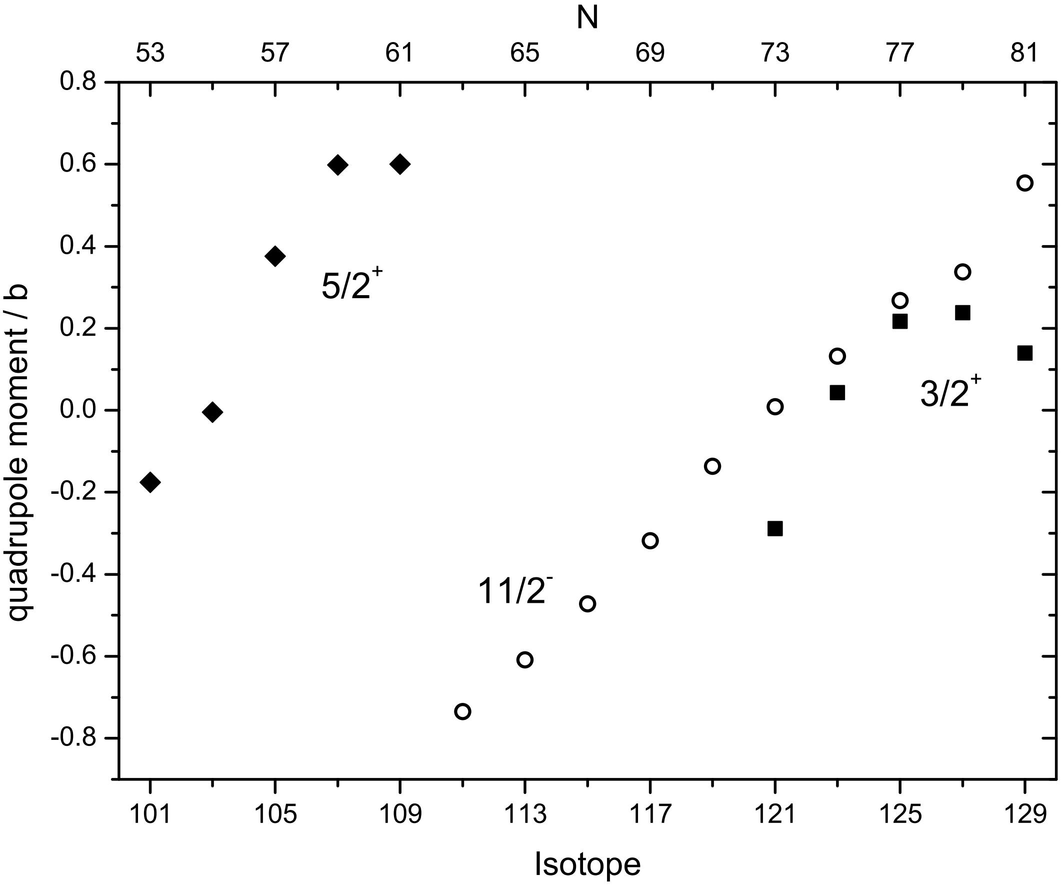

Figure 4.8.: Quadrupole moments of the Cd isotopic chain. The most striking observation is the linear behaviour of the 11/2 state, whith only ^{127}Cd deviating.

calculations as explained in Sec. 2.3, but has never been observed with such significance before. One other occurence is the $I = 11/2$ state in tin isotopes as plotted in Fig. 4.9 on the right. Unexpetedly, in cadmium the trend extends over 10 odd nuclei, equivalent to a capacity of 20 neutrons in the shell. As the natural capacity of the 11/2 shell is 12 neutrons, it has to be extended by sharing pairs with adjacent shells, yet acting exactly like a larger 11/2 shell. The only isotope that exhibits a clear deviation from the linear trend is ^{127}Cd. This might be correlated to the observation of abnormal 2^+ energies as determined by γ-spectroscopy [Rod08] and should be closer investigated.

An empirical single particle moment can be extracted by averaging the single-neutron and single-hole values at the edges

$$Q_{\text{sp}} = \frac{Q(111) - Q(129)}{2} = 644(12)\,\text{mb} \ . \tag{4.5}$$

It can be compared to the shell model value according to Eq. 2.35 using 5/3 of the literature charge radius of ^{111}Cd determined in Sec. 4.3 as radius of the last orbital $Q_{\text{sp}} = e^{\text{eff}} \cdot 291\,\text{mb}$.

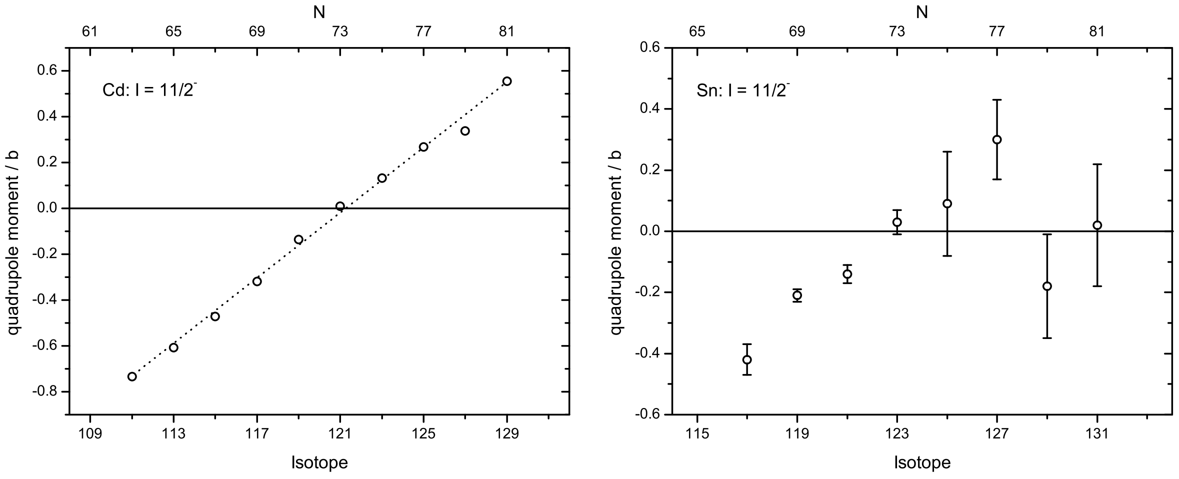

Figure 4.9.: Quadrupole moments of the $I = 11/2$ states of cadmium (left, this work) and tin (right, [At86; Dt75; Le 04]). While Cd shows an almost perfect linear behaviour with only ^{127}Cd deviating, the trend is less significant in Sn.

This leads to a very large effective charge of the neutron of $e_\nu^{\mathrm{eff}} = 2.2e$, which is a sign of strong first-order core polarization. Thus it seems that the missing proton pair makes the Cd-nuclei strongly susceptible to core-polarization.

4.3. Radii

To extract the isotope shift from the measurements of the individual isotopes, one must take into account that the absolute positions extracted in the fitting routine are prone to changes or drifts in the laser frequency, the high voltage at the RFQ and the gas pressure inside the RFQ. Thus, the weighted averages of all ^{114}Cd reference scans directly preceding and succeeding the scan of the relevant isotope are calculated. Those two values are linearly interpolated in time to get the reference frequency at the moment of the measurement, which is then subtracted from the center of gravity of the isotope under investigation. All individual measurements of both runs are averaged, weighted with their statistical uncertainty, to get the final isotope shift for each isotope. The results are presented in Tab. 4.3.

To obtain a reasonable value for the statistical uncertainty of the isotope shift, the ratio between the error resulting from gaussian propagation and the standard error of the mean of the sample is calculated. If it is larger than one, which here usually is the case, the propagated statistical error is increased accordingly. For the small number of isotopes with a number of measurements insufficient to determine the standard error of the mean, the average ratio of all other isotopes is used. Additionally an error of 2.1 MHz is added quadratically. This value is the mean difference from comparison with a completely independent analysis of the same dataset [Yor13a] using, e.g., a different A-factor ratio. It represents the influence of different analysis approaches on the result. The systematic error is calculated according to

$$\begin{aligned}\Delta_{\text{Syst}}(\delta\nu_{\text{IS}}^{A,A'}) =& \nu_0 \left(\frac{eU_{\text{Source}}}{2mc^2}\right)^{1/2} \cdot \\ & \left\{\left(\frac{1}{2}\left(\frac{\delta U_{\text{Scan}}}{U_{\text{Source}}} + \frac{\delta m}{m}\right)\left(\frac{\Delta U_{\text{Source}}}{U_{\text{Source}}}\right)\right)^2 + \right. \\ & \left. \left(\frac{\delta U_{\text{Scan}}}{U_{\text{Source}}}\left(\frac{\Delta(\delta U_{\text{Scan}})}{\delta U_{\text{Scan}}}\right)\right)^2 + \left(\frac{\Delta m}{m}\right)^2\right\}^{1/2} \end{aligned} \tag{4.6}$$

where δ denotes the differences between the different isotopes and Δ denotes the uncertainties. $\Delta U_{\text{Source}}/U_{\text{Source}}$, e. g., is the relative uncertainty of the source voltage. This is derived from the nonrelativistic isotope shift formula [Mt83].

4.3.1. King-plot

The difference in charge radii is linked with the isotope shift by

$$\delta\nu_{\text{IS}}^{A,A'} = K \cdot M + F \cdot \delta\langle r^2\rangle^{A,A'} \tag{4.7}$$

as shown in Sec. 2.1. The mass shift factor K and the electronic field shift factor F for the specific transition can not be extracted solely from optical measurements. Therefore, known charge radii (usually of stable isotopes) are used to perform a so-called King-plot. In this procedure modifying $\delta\langle r^2\rangle$ and $\delta\nu$ with the inverse mass factor results in a straight line with the electronic factor as slope and the mass-shift factor as y-intercept [Kin84]

$$\underbrace{\delta\nu_{\text{IS}}^{A,A'} M^{-1}}_{y} = K + F \cdot \underbrace{\delta\langle r^2\rangle^{A,A'} M^{-1}}_{x} \ . \tag{4.8}$$

In this analysis the radii from [FH04] as listed in Tab. 4.3 were used. They were obtained from the Barrett-radii extracted from muonic measurements using the V_2 coefficient from high energy elastic electron scattering and the relation

$$V_n = R_{k\alpha}\langle r^n\rangle^{-1/n} \ . \tag{4.9}$$

Since the correlation of the systematic errors of the muonic radii is not reported, a worst-case approach is used here assuming them as completely uncorrelated for calculating the $\delta\langle r^2\rangle$[1]. The fit was performed with minuit2 including x- and y-errors. Only statistical errors of the

---

[1] It is expected that the systematic uncertainty of the absolute charge radii will largely cancel when calculating the differences in mean square charge radii $\delta\langle r^2\rangle$.

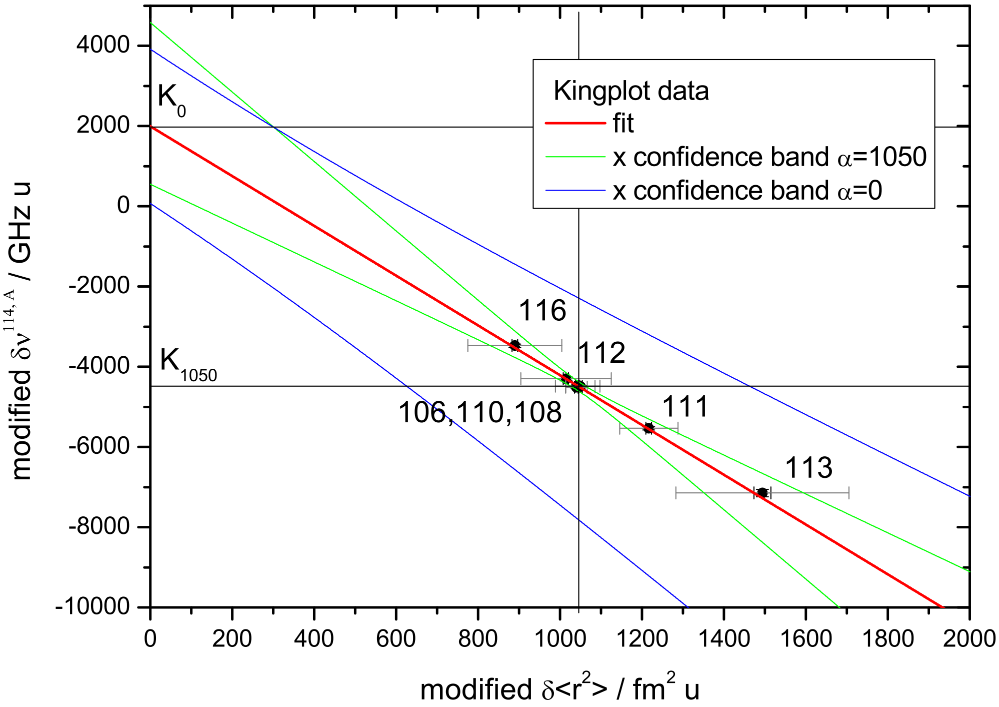

Figure 4.10.: King-plot of the measured Cd isotope shifts against the differences in charge radii of stable isotopes. Small black errors are statistical, the larger grey ones systematical. K_0 shows the mass shift factor at $x = 0$ and the resulting confidence band is shown in blue. It obviously overestimates the uncertainty since the slope and the axis crossing are strongly correlated. This is improved by using K_{1050} as free parameter, leading to the green confidence band which is a much better representation of uncertainties.

data points were used in the first fit to extract the parameters K and F and systematic errors were then added in a second fit to determine the uncertainty of the line parameters. The fact that all points lie almost exactly on the line supports the quality of the data. Only systematic influences that scale as the mass factor M can influence the King-plot without producing deviations from the straight line. The resulting values are

$$\begin{aligned} K_0 =& 1.99(185) \times 10^3 \,\mathrm{GHz\,u} \\ F =& -6.2(18) \,\mathrm{GHz/fm^2} \end{aligned} \tag{4.10}$$

and the corresponding function is shown in Fig. 4.10. The field shift factor agrees very well with the value of $F = -6.1(7) \times 10^3 \,\mathrm{GHz/fm^2}$ obtained in [Bau85] using semi-empirical approaches based on the Landé-Goudsmith-Fermi-Segré formula [Kop56] and the $5s$ hyperfine splitting. Subtracting the normal mass factor of

$$K_{\mathrm{NMS}} = \nu m_{\mathrm{e}} = 0.76 \times 10^3 \,\mathrm{GHz\,u} \tag{4.11}$$

from K results in a specific mass shift of $K_{\mathrm{SMS}} = 1.23(185) \times 10^3\,\mathrm{GHz\,u}$. This is in accordance with the expectation that for an $S \rightarrow P$ transition the specific mass shift is not much larger – rather less – than the normal mass shift.

Unfortunately, due to the fact that the data points are clustered in a single quadrant away from the origin of the plot, the two variables exhibit a strong correlation. This makes accurate calculations of the confidence band and thereby the error in the derived $\delta\langle r^2\rangle$ quite complicated, as this correlation has to be taken into account. Neglecting this and taking simply the linear relation 4.8 using the parameters in 4.10 and gaussian error propagation would result in the 1σ confidence band plotted in 4.10 in blue, which is obviously much too large. This can easily be resolved by fitting a slightly modified line of the form

$$y = K_\alpha + F \cdot (x - \alpha) \ , \tag{4.12}$$

which is equivalent to transforming the coordinate system into one centered at $x = \alpha$. If the parameter α is chosen to be well within the cluster of the modified charge radii, the two degrees of freedom are almost completely decoupled. In this case, $\alpha = 1050\ \mathrm{fm^2u}$ worked best, reducing the correlation parameter from 0.99 to 0.01. The resulting parameters are

$$\begin{aligned} K_{1050} =& -4.52(11) \times 10^3\,\mathrm{GHz\,u} \\ F =& -6.2(18)\,\mathrm{GHz/fm^2} \ . \end{aligned} \tag{4.13}$$

Note that K_α has no physical meaning for $\alpha \neq 0$. As one would expect, the transformation has no influence on the electronic field shift factor, and in general no influence on the line itself, as K_{1050} results simply in $K_{1050} = K_0 + F \cdot 1050$. But the relative uncertainty of K becomes smaller, and the Gaussian error propagation of the uncertainties in K and F to an error in the modified $\delta\langle r^2\rangle$ leads to the confidence band plotted in Fig. 4.10 in green, which describes the data much better.

The new King-plot equation leads to

$$\delta\langle r^2\rangle^{A,A'} = \left(\delta\nu_{\mathrm{IS}}^{A,A'} - K_\alpha M\right)/F + \alpha M \ . \tag{4.14}$$

The $\delta\langle r^2\rangle$ extracted from the isotope shifts are listed in Tab.4.3 and shown in Fig.4.11. The radii of $^{117-120,122}$Cd are taken from [Fr3] due to inappropriate conditions during the experiment as explained in Sec. A.3.The statistical error is $\Delta_{\mathrm{stat}}(\delta\langle r^2\rangle) = (1/F) \cdot \Delta(\delta\nu)$. The systematic error of $\delta\langle r^2\rangle$ includes the systematic error of $\delta\nu$, the isotope mass uncertainty

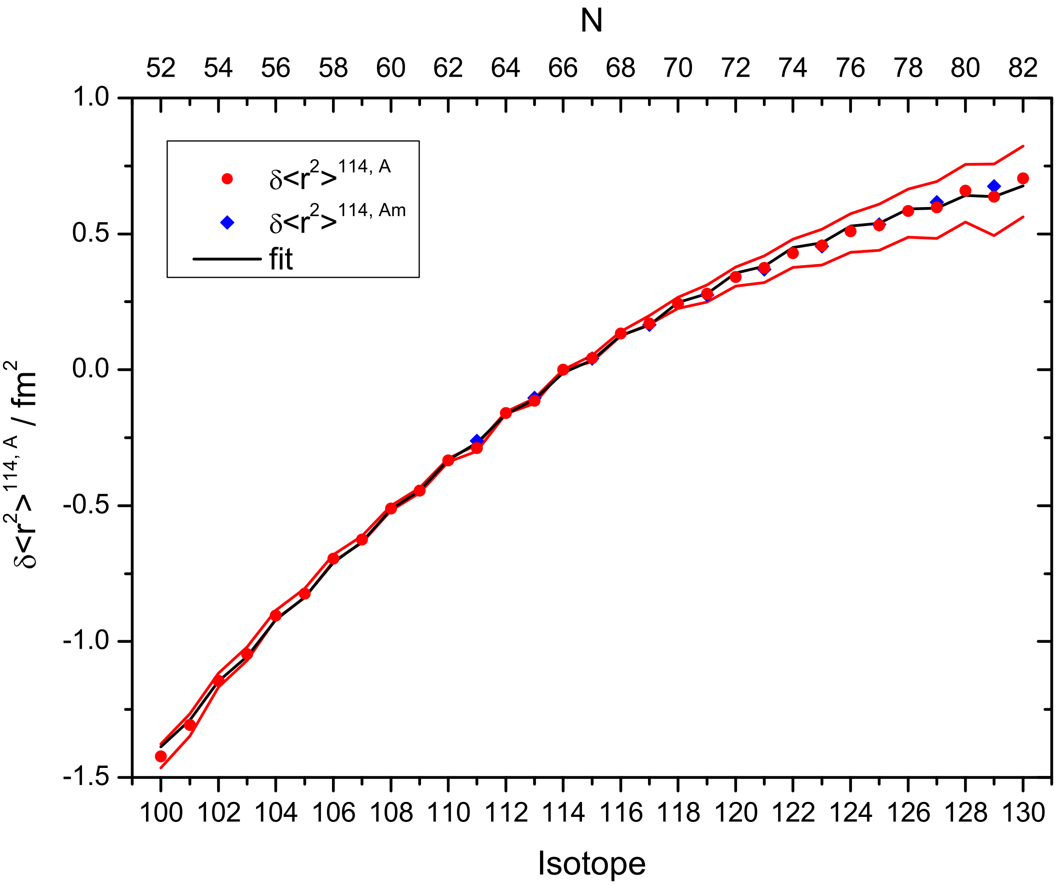

Figure 4.11.: Differences in mean square charge radii of cadmium for the ground state (red) and the isomeric state (blue) as obtained from this run and the atomic one[Fr3]. Statistic errors are smaller than the symbols and therefore not plotted. The red confidence band shows the systematic error. The black line is a fit of the parametrization of Zamick and Thalmi to the data. Details are discussed in the text.

and the error from the King-plot parameters according to gaussian error propagation from 4.14:

$$\Delta_{\mathrm{syst}}(\delta\langle r^2\rangle) = \Bigg\{ \left(\frac{1}{F}\Delta_{\mathrm{syst}}(\delta\nu)\right)^2 + \left(\frac{M}{F}\Delta K\right)^2 + \left((\delta\nu - KM)\frac{1}{F^2}\Delta F\right)^2 + \left(\left(\frac{K}{F}+\alpha\right)\frac{1}{m_{114}^2}\Delta m_A\right)\Bigg\}^{1/2} . \qquad (4.15)$$

The reason for the larger systematic errors on the neutron-rich side can easily be understood by the modified isotope shift of the different nuclei, as visualized in Fig. 4.12. The blue points denote the reference isotopes with known ms charge radii used for the King-plot, which is consequently the region in the King-plot, where the confidence band is smallest. While the neutron-deficient isotopes stay close to this range, the neutron-rich isotopes systematically

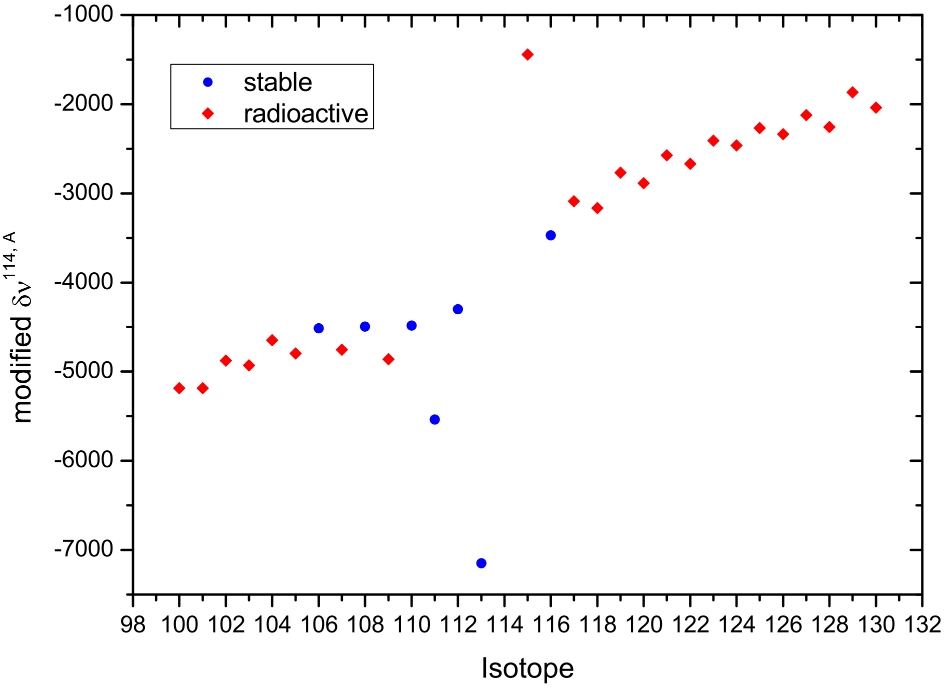

Figure 4.12.: Modified isotope shift of the different isotopes measured in this work. The isotopes with charge radii used as reference in the King-plot procedure are marked blue. As one can see, the modified isotope shifts of neutron deficient isotopes are close to the reference values, while the neutron rich ones evolve further away. This causes the difference in the uncertainties of charge radii between those nuclei.

develop to higher modified isotope shifts and therefore into an area of the King-plot with larger uncertainties.

The radii of the ground state expose a linear growth with an additional parabolic shape with positive curvature spanning from one shell closure to the other. On top of this, a regular odd-even staggering is superimposed i.e. isotopes with an odd number of neutrons have radii smaller than the average of the neighbouring even N isotopes. This behaviour fits well to the differences in charge radii of the surrounding elements and can be described and interpreted in the framework of Zamick and Thalmi [Zam71; Tal84]. There, the curve is parameterized as

$$\delta\langle r^2\rangle = a(N-50) + b(N-50)(82-N) + \frac{c}{2}\left[1-(-1)^N\right] + d \tag{4.16}$$

and fitted to the data points. The parameters seperate the change in radius due to the volume effect a, a deformation due to core-polarization peaking in mid-shell b, the odd-even staggering c and an offset due to the choice of reference d.

The fit results in a size of the volume effect of $a = 0.072$ fm^2, which is in very good agreement with the value of the droplet model [MS83][BT85] of $a = 0.074$ fm^2. The obtained value of $b = 0.0017$ fm^2 leads to a maximum $\delta\langle r^2\rangle_{\text{def}} = b(16^2) = 0.445$ fm^2 due to deformation

$Z+N$	I	$\delta\nu_{\mathrm{IS}}^{114,A}$	$\delta\langle r^2\rangle^{114,A}$	$\sqrt{\langle r^2\rangle_{\mathrm{Lit}}}$	$\delta\langle r^2\rangle_{\mathrm{Lit}}^{114,A}$
100	0	6371.6(31)[114]	-1.4218(5)[0436]		
101	5/2	5859.9(22)[105]	-1.3075(4)[0402]		
102	0	5037.2(22)[096]	-1.1438(3)[0253]		
103	5/2	4621.6(24)[087]	-1.0462(4)[0245]		
104	0	3922.7(24)[079]	-0.9036(4)[0161]		
105	5/2	3608.7(22)[070]	-0.8235(4)[0167]	4.53631(31)[133]	-0.6893(29)[172]
106	0	2991.1(22)[062]	-0.6952(4)[0121]		
107	5/2	2730.9(23)[054]	-0.6248(4)[0121]	4.55577(23)[133]	-0.5124(23)[172]
108	0	2194.0(22)[046]	-0.5105(4)[0089]		
109	5/2	1958.3(22)[038]	-0.4451(4)[0096]	4.57539(16)[133]	-0.3333(16)[173]
110	0	1432.2(23)[030]	-0.3335(4)[0059]	4.58025(16)[125]	-0.2888(16)[168]
111	1/2	1314.3(22)[023]	-0.2881(4)[0118]	4.59437(08)[133]	-0.1592(10)[173]
112	0	674.6(22)[015]	-0.1592(4)[0033]	4.59907(16)[117]	-0.1160(16)[163]
113	1/2	555.2(23)[008]	-0.1145(4)[0094]	4.61167(08)[133]	0.0000(00)[000]
114	0	0.0(0)[000]	0.0000(0)[0000]		
115	1/2	-110.4(29)[007]	0.0424(5)[0109]	4.62627(08)[133]	0.1349(10)[174]
116	0	-526.5(22)[015]	0.1336(3)[0078]		
117	1/2		0.1698(5)[0195]		
118	0		0.2434(5)[0206]		
119	1/2		0.2802(16)[0314]		
120	0		0.3415(12)[0351]		
121	3/2	-1309.3(40)[050]	0.3746(6)[0463]		
122	0		0.4297(3)[0511]		
123	3/2	-1551.5(37)[065]	0.4570(6)[0633]		
124	0	-1748.2(22)[072]	0.5098(4)[0680]		
125	3/2	-1757.3(35)[079]	0.5321(6)[0810]		
126	0	-1957.6(22)[086]	0.5849(3)[0852]		
127	3/2	-1912.3(30)[094]	0.5978(5)[1002]		
128	0	-2171.6(23)[100]	0.6594(4)[1013]		
129	3/2	-1911.1(55)[108]	0.6370(9)[1256]		
130	0	-2208.1(33)[115]	0.7041(5)[1246]		
111	11/2	1148.8(22)[023]	-0.2615(4)[0055]		
113	11/2	489.0(22)[008]	-0.1038(4)[0065]		
115	11/2	-100.6(29)[007]	0.0408(5)[0113]		
117	11/2		0.1660(1)[0206]		
119	11/2		0.2755(15)[0327]		
121	11/2	-1277.3(31)[050]	0.3695(5)[0478]		
123	11/2	-1532.7(28)[063]	0.4540(5)[0641]		
125	11/2	-1772.6(26)[077]	0.5346(4)[0803]		
127	11/2	-2029.1(24)[092]	0.6166(4)[0949]		
129	11/2	-2145.5(31)[105]	0.6748(5)[1150]		

Table 4.3.: Isotope shifts $\delta\nu_{\mathrm{IS}}^{114,A}$ and extracted mean square charge radii from this work and literature values from [FH04]. Results for $^{117-120,122}$Cd are taken from [Fr3] due to inappropriate conditions during the experiment as explained in Sec. A.3.

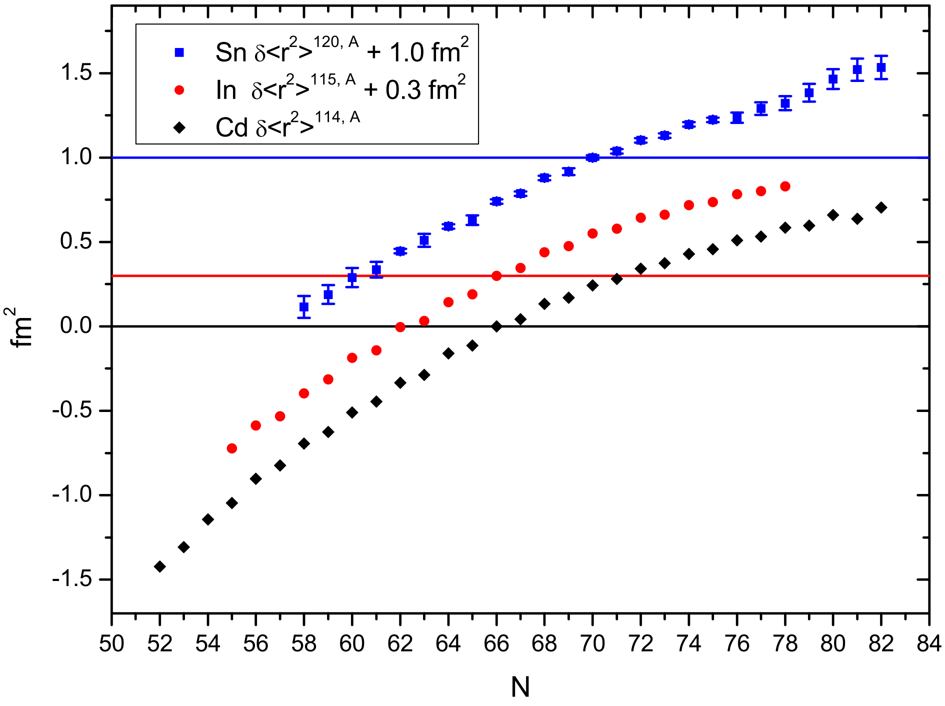

Figure 4.13.: Differences of mean square charge radii of cadmium (this work), indium [FH04] and tin [FH04][Le 05]. The latter two are shifted for better visibility. The dip around $N = 78$ in tin isotopes is caused by the stitching of the two datasets.

in midshell, according to a deformation of $\langle\beta^2\rangle = 0.054$ following Eq. 2.40. The remaining parameters are $c = -0.025$ fm^2 and $d = -0.453$ fm^2.

The $11/2^-$ state follows roughly the same behaviour. In Fig. 4.11 the points practically with those of the ground state. Only at the edges of the isomer existence the points deviate slightly from the ground state. A closer look at the difference reveals a very interesting behaviour: As can be seen in Fig. 4.14, the difference in charge radius forms a parabola over the entire 11/2 shell centered around ^{120}Cd. While the isomer is larger at the shell borders, it becomes smaller than the ground state in midshell, where additionally the ground state changes its spin from 1/2 to 3/2. It is not clear whether this trend continues beyond ^{111}Cd, where the 7/2 state becomes lower in energy than the 11/2 state and the latter one therefore is short-lived. This interesting behaviour currently is under further investigation. One approach is to interpret the difference in charge radius as difference in deformation, which leads to a variation in $\delta\langle\beta^2\rangle^{A,Am}$ between 0.004 and -0.0006.

In Fig. 4.15 the radii obtained in this work are compared to first results of theoretical calculations of the even isotopes [Rod13] triggered by this work. The Gogny-force [Bt84] in a standard parametrization (D1S) and one improved for masses (D1M) are used in a mean-field (MF) and a beyond-mean-field (BMF) [Rod08] approach. These calculations predict a larger variation of charge radii than is experimentally observed, but expose a similar curvature.

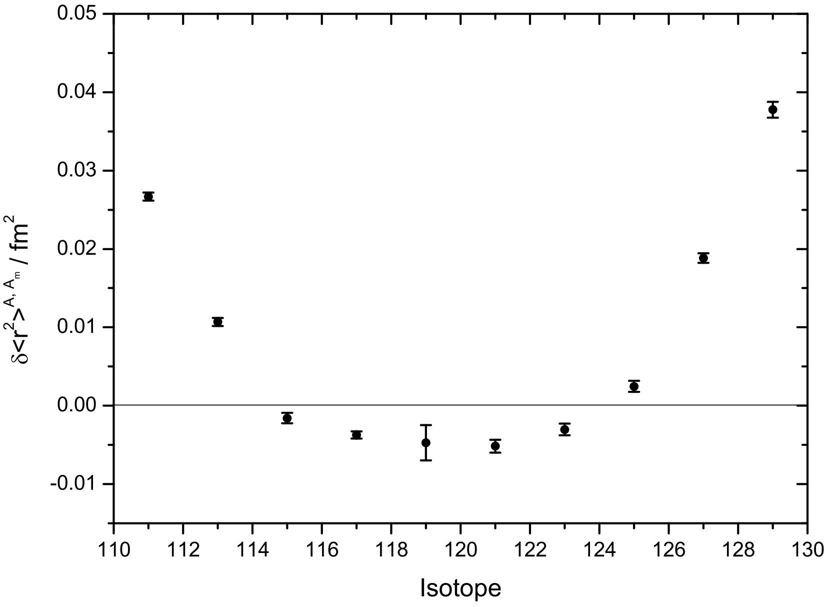

Figure 4.14.: Difference in mean square charge radius between ground and 11/2 isomeric state. The large error of ^{119}Cd is caused by an unfortunate overlap of hyperfine lines of ground and isomeric state in the atomic system.

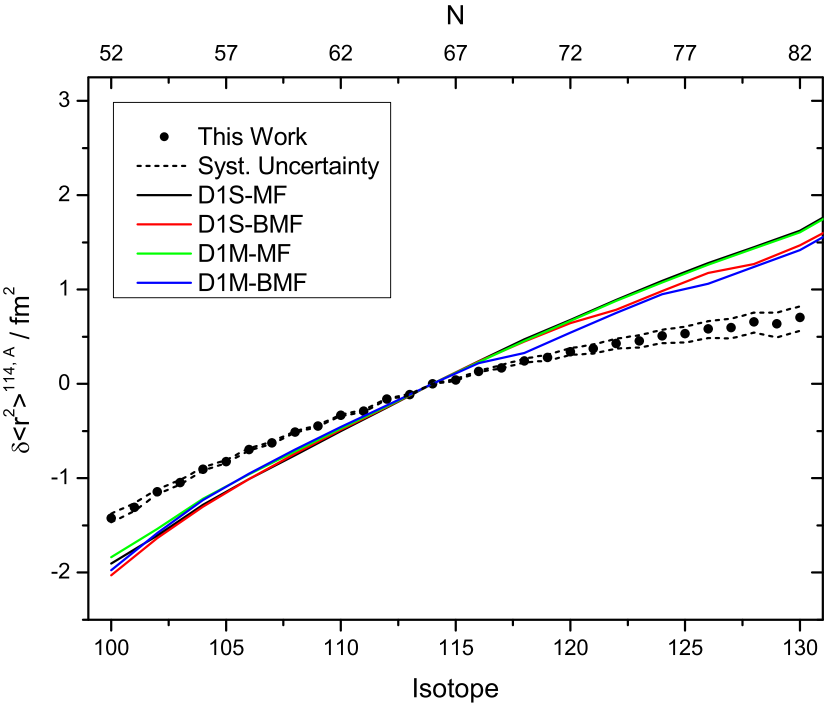

Figure 4.15.: Comparison of differences in ms charge radius to theoretical calculations of the even Cd isotopes. Two parametrizations of the Gogny-force (D1S and D1M) are used in combination with mean-field (MF) and beyond-mean-field (BMF) calculations.

The difference is significant in respect to the difference between methods as well as the experimental systematic error. Similar calculations for the odd isotopes as well as calculations using a Skyrme force [Rei11] are in progress. This demonstrates the value of experimentally observed nuclear ground state properties as measure for theoretical calculations to improve the understanding of nuclear structure.

5. Summary and Outlook

Detection efficiency is a crucial topic in order to expand laser spectroscopy towards more and more exotic species. In this thesis a boost in efficiency for the spectroscopy of Cd isotopes has been reached by building a continuous-wave laser system at 214.6 nm and by using the radiofrequency cooler and buncher ISCOOL. This allowed to extend the previously performed collinear laser spectroscopy on neutral $^{106-126}$Cd to cover the $100 \leq A \leq 130$ chain, getting close to $N = 50$ on the neutron-deficient side and ultimately reaching the $N = 82$ shell closure. The resulting spectra were analyzed and magnetic dipole and electric quadrupole moments as well as differences in mean square nuclear charge radii have been extracted. Those experimental observables give valuable insight into the nuclear structure of systems in the vicinity of closed shells around the doubly magic nuclei ^{100}Sn and ^{132}Sn.

The change in mean-square nuclear charge radii along the isotopic chain is smooth and the general trend can be well described within the droplet model. Also the Zamik-Thalmi model can be fitted very well to the data reproducing the regular odd-even staggering and the curvature. An interesting behaviour is revealed by the measured differences in mean square charge radii between ground and isomeric state, where a parabolic behaviour can be observed. Among the most striking observations is the linear dependence of the quadrupole moment on the neutron number in the $11/2^-$ shell, which is valid over a sequence of 20 neutrons and therefore longer than the estimated capacity of the shell. For a complete interpretation of the observed effects, more input, especially from theoretical calculations, is necessary. These observations have triggered self-consistent mean-field calculations with Gogny and Skyrme forces for the Cd isotopes but only with limited success so far. Similar trends for quadrupole moments have also been observed.

Currently a prosposal [Yor13b] has been submitted to extend the measurements to ^{99}Cd and ^{131}Cd. This would provide nuclear ground state properties of two more neutron single-particle states and, by crossing the $N = 82$ shell closure, will bring clarity to the matter of the visibility of shell effects in charge radii in this mass region. Additionally, the measurement of Sn$^{104-136}$ and its isomers is proposed, eventually on the 215 nm line due to its high sensitivity, using the laser system described in this work. By measuring the nuclei of tin with the same neutron states as in Cd but with a closed proton shell, it will be possible to evaluate the influence of the missing proton pair on the nuclear properties. Further extensions of those measurements to even heavier nuclei like Te with one proton pair beyond the shell closure should improve the knowledge about the Z-dependence of the observed phenomena.

A. Appendix

A.1. Masses

The masses of the isotopes used for the evaluation in this work are listed in Tab. A.1. To extract the mass of the ion, one electron mass has to be subtracted from the listed one. The values are taken from AME [WA12] and newer penning trap mass measurements [Kan12] where available. The latter are marked by an asterisk in the table. For ^{127}Cd and ^{129}Cd, where neither the isomeric mass nor the spin is known, the mass of the ground state was used and the uncertainty was estimated as the largest excitation energy of the known isomers in the vicinity, namely 300 keV.

A.2. Comparison of Nuclear Moments

In Fig. A.1, A.2, A.3 and A.4 the differences between moments obtained in this work, the atomic run and literature are plotted. The overall agreement is good. The systematic deviation from literature quadrupole moments can be attributed to a different V_{zz}.

A.3. Comparison of Radii

The differences in the mean square charge radii measured in the ionic transition are compared to the literature values (as used for the King plot) and the radii from the atomic transition in Fig. A.5. Only statistical errors are shown. One can see that the literature values agree very well, as expected. While most of the atomic radii are within the statistical limits as well, the neutron rich isotopes starting from ^{123}Cd start to deviate systematically. This observed behaviour is caused by small differences in the mass and field shift factors between the two runs and is a residual effect which is well within the systematic error bars, which are not shown as they are one to two orders of magnitude larger than the statistical ones. Furthermore the isotopes $^{117-120}$Cd and ^{122}Cd obviously deviate more than expected and the behaviour can be hardly explained by the King-plot procedure. This is discussed in the following paragraphs. One should note that those isotope shifts are not included in our results in Tab 4.3.

$Z+N$	I	m / u
100	0	99.9203488(2)
101	5/2	100.9185865(2)
102	0	101.9144818(2)
103	5/2	102.9134163(2)
104	0	103.9098562(2)
105	5/2	104.9094638(1)
106	0	105.9064617(2)
107	5/2	106.9066123(2)
108	0	107.9041835(2)
109	5/2	108.9049867(2)
110	0	109.9030049(2)
111	1/2	110.9041811(2)
112	0	111.9027608(2)
113	1/2	112.9044047(2)
114	0	113.9033616(2)
115	1/2	114.9054340(2)
116	0	115.9047589(2)
117	1/2	116.9072217(2)
118	0	117.9069177(22)
119	1/2	118.9098469(40)
120	0	119.9098681(4)
*121	3/2	120.9129809(91)
122	0	121.9134546(5)
*123	3/2	122.9169949(40)
124	0	123.9176619(10)
*125	3/2	124.9212578(65)
126	0	125.9224295(5)
127	3/2	126.9265316(329)
128	0	127.9278038(18)
129	3/2	128.9320300(384)
130	0	129.9339360(177)
111	11/2	110.9046065(2)
113	11/2	112.9046877(2)
115	11/2	114.9056284(2)
117	11/2	116.9073682(2)
119	11/2	118.9100043(40)
*121	11/2	120.9132116(91)
*123	11/2	122.9171495(40)
*125	11/2	124.9214575(66)
127	11/2	126.9265316(329)
129	11/2	128.9320300(384)

Table A.1.: Masses used in the analysis of this work. Values originate from the atomic mass evaluation [WA12] and, where available, newer penning trap mass measurements [Kan12], which are marked by an asterisk.

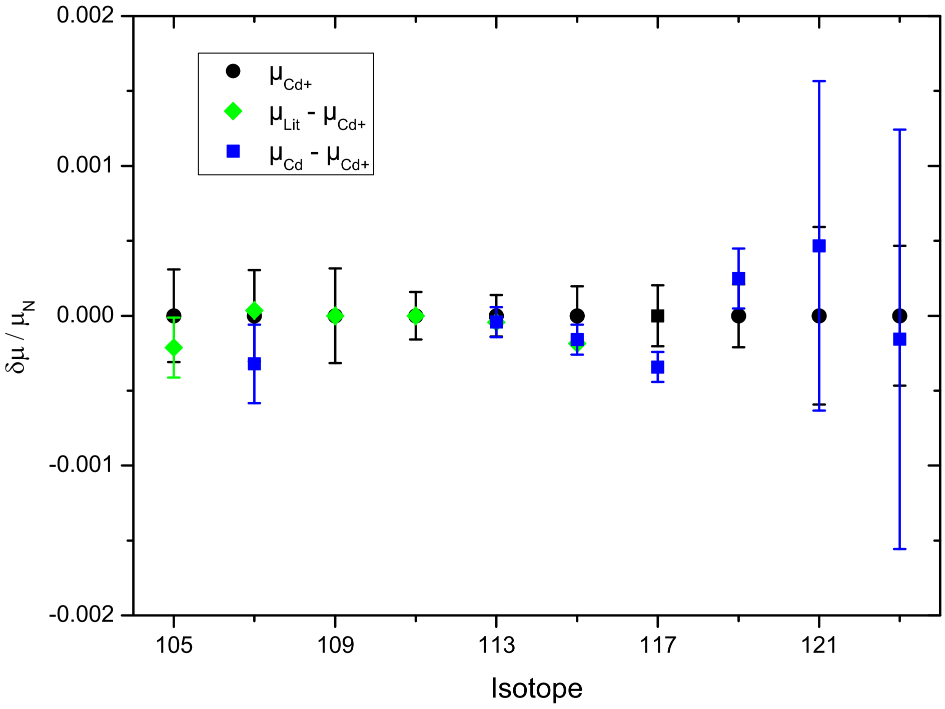

Figure A.1.: Comparison of magnetic moments of the low spin state of this work (black), the previous spectroscopy on neutral cadmium (blue) and known literature values [Sto05], as listed in Tab. 4.1.

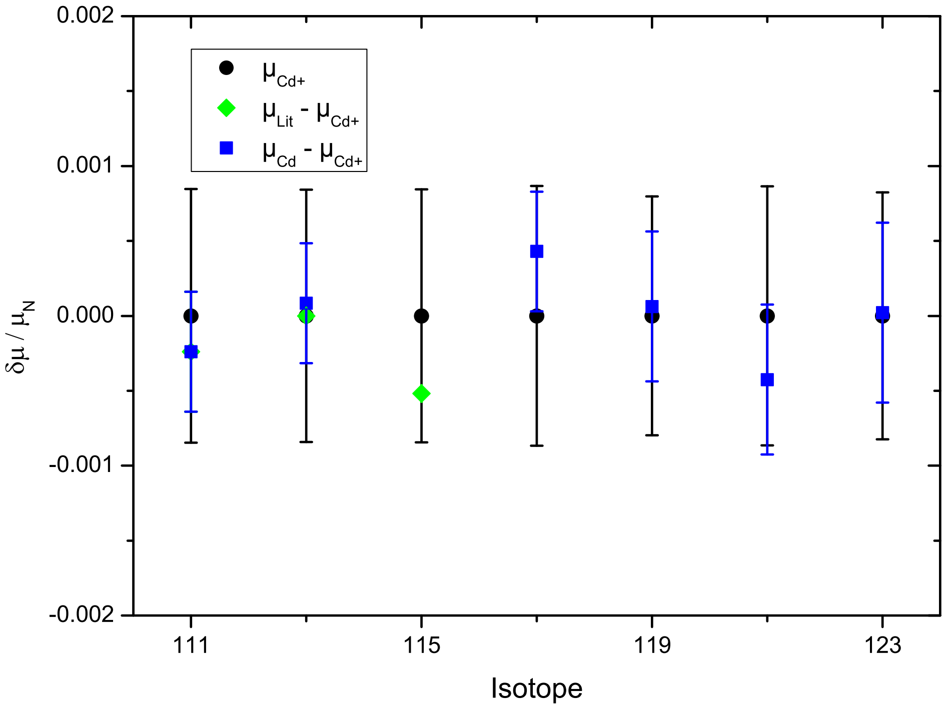

Figure A.2.: Comparison of magnetic moments of the 11/2 spin state of this work (black), the previous spectroscopy on neutral cadmium (blue) and known literature values [Sto05], as listed in Tab. 4.1.

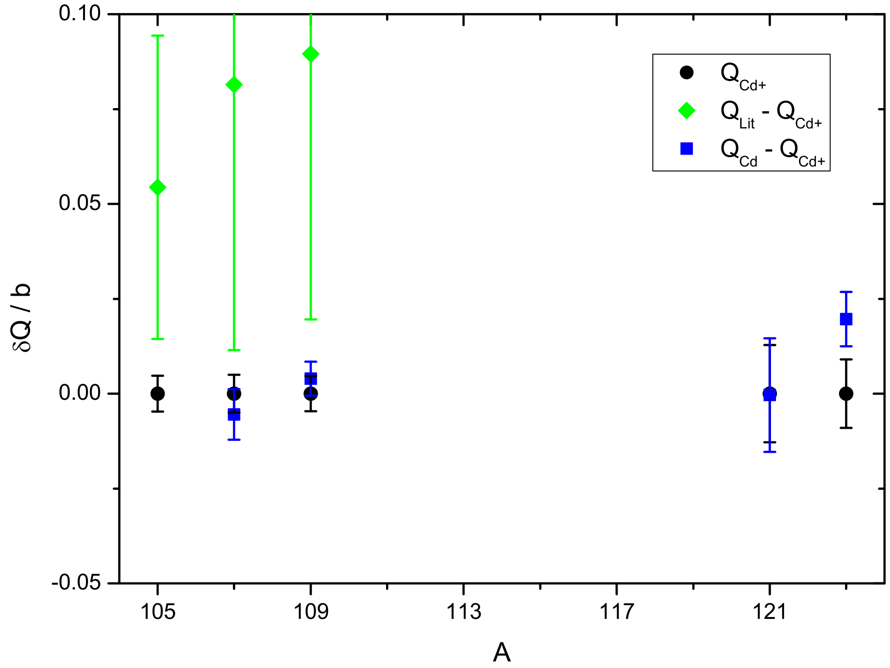

Figure A.3.: Comparison of quadrupole moments of the low spin state of this work (black), the previous spectroscopy on neutral cadmium (blue) and known literature values [Sto05], as listed in Tab. 4.2. The deviation from literature values is caused by a different V_{zz}.

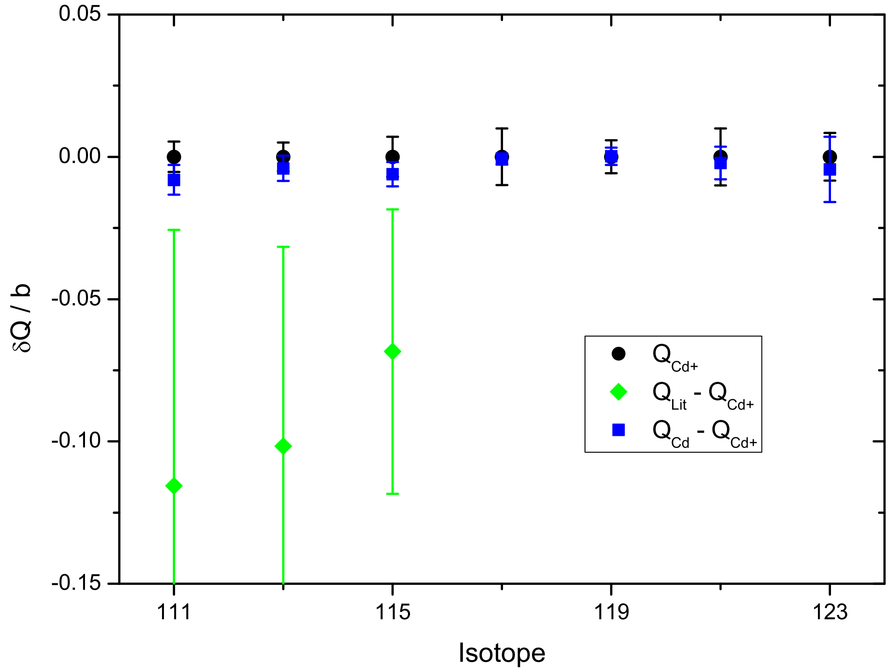

Figure A.4.: Comparison of quadrupole moments of the 11/2 spin state of this work (black), the previous spectroscopy on neutral cadmium (blue) and known literature values [Sto05], as listed in Tab. 4.2. The deviation from literature values is caused by a different V_{zz}.

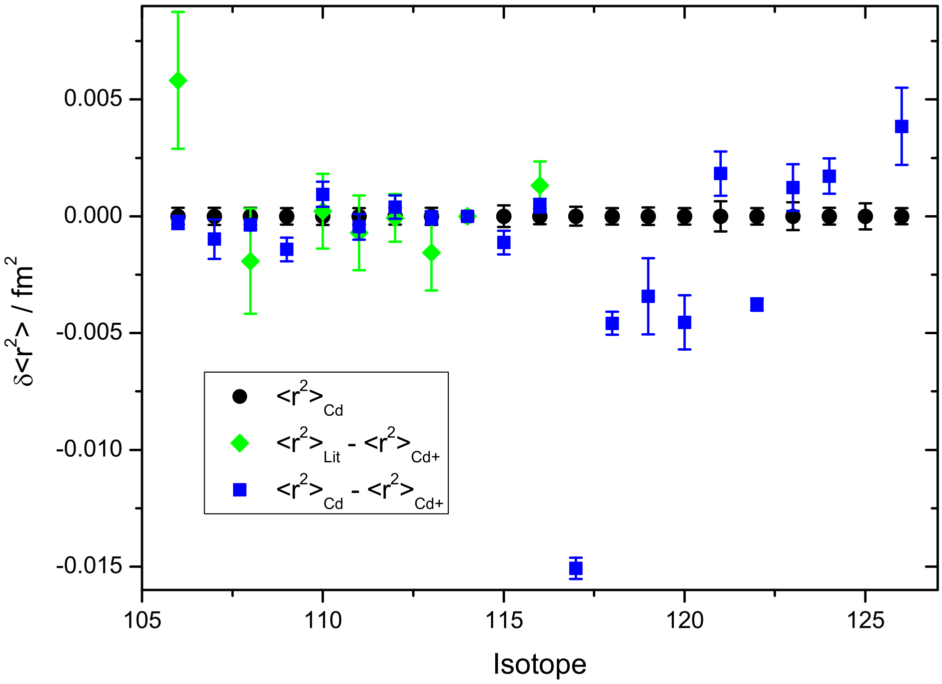

Figure A.5.: Comparison of differences in mean square charge radius from this work, literature values and the atomic run on Cd. The shown error bars are statistical errors only. The overall agreement is very good. The deviation between ion and atom data on the neutron deficient side can be explained by systematics from the King plot, while for the isotopes $^{117-120}$Cd and ^{122}Cd systematic deviations must have happened during the experiment. An explanation for these effects is given in Fig. A.6.

Only one single spectrum of each of the isotopes $^{117-120}$Cd and ^{122}Cd has been taken at the very end of the experiment, as they have been measured during the atomic run and general agreement between the sets has already been ascertained with ^{123}Cd, ^{124}Cd and ^{126}Cd. Therefore it was not the primary goal of the run and only some spare time after successfully measuring all necessary isotopes was used. The deviation of ^{117}Cd corresponds to about 90 MHz in isotope shift. Additionally, the measurement of ^{112}Cd done at the very end is about 15 MHz off to the earlier ones. Obviously during that time something influenced the isotope shifts in a systematic way much more than would normally be expected. A comparison of the measured source voltage and the line center of the reference isotope ^{114}Cd, as shown in Fig. A.6, reveals some interesting behaviour. During most of the run the transition frequency follows the measured source voltage quite well, indicating that indeed it is the power supply that is drifting a bit during this time (left). This effect is smaller than the accuracy of our voltage measurement and the assumed error. Yet in the end, where the other isotopes have been measured, the transition frequency changes without an according change of the source voltage by about 25 MHz. As the laser system was perfectly stable, this has to be related to

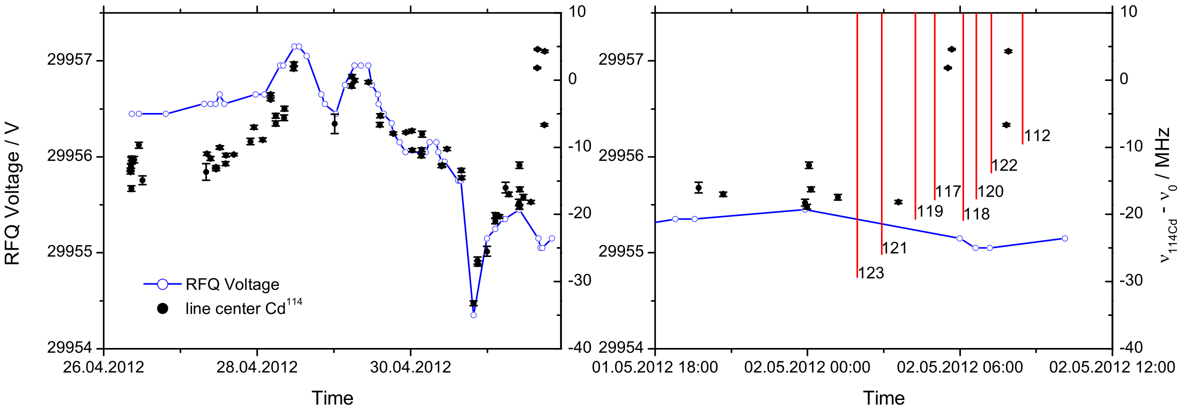

Figure A.6.: RFQ voltage and reference line center during the whole run on neutron deficient Cd (left) and in detail only the end of the run (right). Most of the time the line center of the reference follows the voltage quite well, indicating that the high voltage power supply is drifting. Yet, in the end both clearly deviate, exactly where the measured isotope shifts disagree with the result of the atomic beamtime. The measurement times for the different exotic isotopes that were measured at the end of the run are indicated by red lines.

a change in ion velocity. Normally, one would expect this shift to cancel out to a large degree in the difference between two isotopes, but this does not seem to happen.

As the beam energy is purely determined by potential of the radiofrequency quadrupole cooler and buncher, it is the most obvious candidate for a malfunction. After the according run, the gas bottle supplying the buffer gas was almost empty. Unfortunately, the pressure cannot be monitored while high voltage to the platform is applied. Taking all the facts into account, the most probable explanation for the observed behaviour is a change in buffer gas pressure inside the radiofrequency cooler and buncher. Outside its working parameters, cooling is insufficient and the capacity of the rfq is suspected to drop. Overloading might occur much earlier and the ion velocity can depend on the number of ions inside the bunch. Unfortunately, it is not possible to verify this assumption. These observations show how critical systematic investigations and proper control of working parameters of the radiofrequency cooler and buncher are for collinear laser spectroscopy.

Bibliography

[At86] M. Anselment *et al.*, *Charge radii and moments of tin nuclei by laser spectroscopy*, Physical Review C **34** (1986), 1052.

[Bau85] J. Bauche *et al.*, *Analysis of Optical Isotope Shifts in Cadmium*, Zeitschrift fuer Physik A **320** (1985), 157–163.

[BF13] J. Bieroń and S. Fritzsche, *private communication*, 2013.

[Bla13] K. Blaum *et al.*, *Precision atomic physics techniques for nuclear physics with radioactive beams*, Physica Scripta **152** (2013), 32.

[Bt84] J. F. Berger *et al.*, *Microscopic analysis of collective dynamics in low energy fission*, Nuclear Physics A **428** (1984), 23c.

[BT85] D. Berdichevsky and F. Tondeur, *Nuclear Core Densities, Isotope Shifts, and the Parametrization of the Droplet Model*, Zeitschrift für Physik A **332** (1985), 141–147.

[BWW01] K. Bethge, G. Walter, and B. Wiedemann, *Kernphysik*, Springer, 2001.

[Cat03] R. Catherall *et al.*, *Radioactive ion beams produced by neutron-induced fission at ISOLDE*, Nuclear Instruments and Methods B **204** (2003), 235–239.

[Dem05] W. Demtröder, *Experimentalphysik 3*, Springer, 2005.

[Dem07] W. Demtröder, *Laserspektroskopie*, Springer, 2007.

[Dra06] G. Drake, *Atomic, Molecular and Optical Physics*, Springer, 2006.

[Dt75] F. Dimmling *et al.*, *Quadrupole moments of ν h11/2 states in Sn-isotopes and electric field gradients at the Sn and Cd sites in Cd, Sn and Sb metal*, Physics Letters **55B** (1975), 293.

[FH04] G. Fricke and K. Heilig, *Nuclear Charge Radii*, Landolt-Börnstein, Springer, 2004.

[Fr3] N. Frömmgen, *Kollineare Laserspektroskopie an radioaktiven Praseodymionen und Cadmiumatomen*, Ph.D. thesis, Johannes Gutenberg-Universität Mainz, 2013.

[GMJ55] M. Goeppert Mayer and J. H. D. Jensen, *Elementary Theory of Nuclear Shell Structure*, John Wiley & Sons, 1955.

[Gor13] C. Gorges, *Verbesserung des optischen Nachweises und Charakterisierung gebunchter Ionenstrahlen am TRIGA-SPEC Experiment in Mainz*, Master's thesis, Johannes Gutenberg-Universität Mainz, 2013.

[Gra94] I. P. Grant, *Relativistic calulation of atomic properties*, Computer Physics Communications **84** (1994), 59.

[ISO13] ISOLDE, ISOLDE homepage, 2013.

[Jt07] P. Jönsson *et al.*, *The GRASP2K relativistic atomic structure package*, Computer Physics Communications **176** (2007), 597.

[Jt13] P. Jönsson *et al.*, *New version: GRASP2K relativistic atomic structure package*, Computer Physics Communications **184** (2013), 2197.

[KÖ3] U. Köster, *On-line yields obtained with the ISOLDE RILIS*, Nuclear Instruments and Methods B **204** (2003), 347–352.

[Kan12] A. Kankainen, *Isomeric states close to doubly magic 132sn studied with jyfltrap*, Physical Review C **87** (2012), 024301.

[Kau76] S.L. Kaufman and F.U. Horst, *High-resolution laser spectroscopy in fast beams*, Optics Communications **17** (1976), no. 3, 309–312.

[Kin84] W. H. King, *Isotope shifts in atomic spectra*, Plenum Press New York and London, 1984.

[Kop56] Kopfermann, *Kernmomente*, Akad. Verlagsanstalt, 1956.

[Kre13] K. D. Kreim, *Collinear Laser Spectroscopy of Potassium*, Ph.D. thesis, Ruprecht-Karls-Universitat Heidelberg, 2013.

[Kri12] A. Krieger, *Laser systems for collinear spectroscopy and the charge radius of 12Be*, Ph.D. thesis, Johannes Gutenberg-Universität Mainz, 2012.

[Kt08] U. Köster *et al.*, *Progress in ISOL target-ion source systems*, Nuclear Instruments and Methods B **266** (2008), 4229–4239.

[Le 04] F. Le Blanc *et al.*, *Charge Radii and Nuclear Moments around 132Sn*, Nuclear Physics A **734** (2004), 437.

[Le 05] F. Le Blanc *et al.* , *Charge-radius change and nuclear moments in the heavy tin isotopes from laser spectroscopy: Charge radius of 132Sn*, Physical Review C **72** (2005), 034305.

[Man09] E. Mané, *An ion cooler-buncher for high-sensitivity collinear laser spectroscopy at ISOLDE*, European Physics Journal A **42** (2009), 503–507.

[MS83] W. D. Meyers and K.-H. Schmidt, *An update on droplet-model charge distributions*, Nuclear Physics A **410** (1983), 61–73.

[Mt83] F. Mueller *et al.*, *Spins, moments and charge radii of barium isotopes in the range 122-146Ba determined by collinear fast-beam laser spectroscopy*, Nuclear Physics A **403** (1983), no. 2, 234–262.

[Nat13] National Nuclear Data Center, *NuDat 2.6*, 2013.

[Ney03] G. Neyens, *Nuclear magnetic and quadrupole moments for nuclear structure research on exotic nuclei*, Reports on Progress in Physics **66** (2003), 633–689.

[NIS12] NIST, *NIST Atomic Database*, 2012.

[NN06] R. Neugart and G. Neyens, *Nuclear Moments*, Lecture Notes in Physics **700** (2006), 135–189.

[Ott89] E.W. Otten, *Nuclear radii and moments of unstable isotopes*, Treatise on heavy-ion science **8** (1989), 517–638.

[Pea89] B. M. Peake, *The discovery of the electron, proton, and neutron*, Journal of Chemical Education **66** (1989), 738.

[Rei11] P. G. Reinhard, *Self-consistent nuclear mean-field models: example Skyrme-Hartee-Fock*, Journal of Physics G **38** (2011), 43.

[Rod08] T. R. Rodríguez, *On the origin of the anomalous behaviour of* 2^+ *excitation energies in neutron-rich Cd isotopes*, Physics Letters B **668** (2008), 410 – 413.

[Rod13] T. R. Rodríguez, *private communication*, 2013.

[Rut11] E. Rutherford, *The Scattering of* α *and* β *Particles by Matter and the Structure of the Atom*, Philosophical Magazine **21** (1911), 669.

[SH08] C. P. Schulz and I. V. Hertel, *Atome, Moleküle und optische Physik*, Springer, 2008.

[ST07] B. E. A. Saleh and M. C. Teich, *Fundamentals of Photonics*, Wiley, 2007.

[Sto05] Stone, N. J., *Table of nuclear magnetic dipole and electric quadrupole moments*, Atomic Data and Nuclear Data Tables **90** (2005), 75–176.

[Tal84] I. Talmi, *On the odd-even effect in the charge radii of isotopes*, Nuclear Physics A **423** (1984), 189–196.

[WA12] M. Wang and G. Audi, *Atomic Mass Evaluation 2011 preview, private communication*, 2012.

[Yor13a] D. T. Yordanov, *Private communication*, 2013.

[Yor13b] D. T. Yordanov *et al.*, *CERN-INTC-2013-014*, 2013.

[Yor13c] D.T. Yordanov *et al.*, *Spins, Electromagnetic Moments, and Isomers of 107 - 129 Cd*, Physical Review Letters **110** (2013), 192501.

[Zam71] L. Zamick, *Two Body Contribution of the Effective Radius Operator*, Annals of Physics **66** (1971), 784–789.